Cell

High expression of oleoyl-ACP hydrolase underpins life-threatening respiratory viral diseases

Graphical abstract

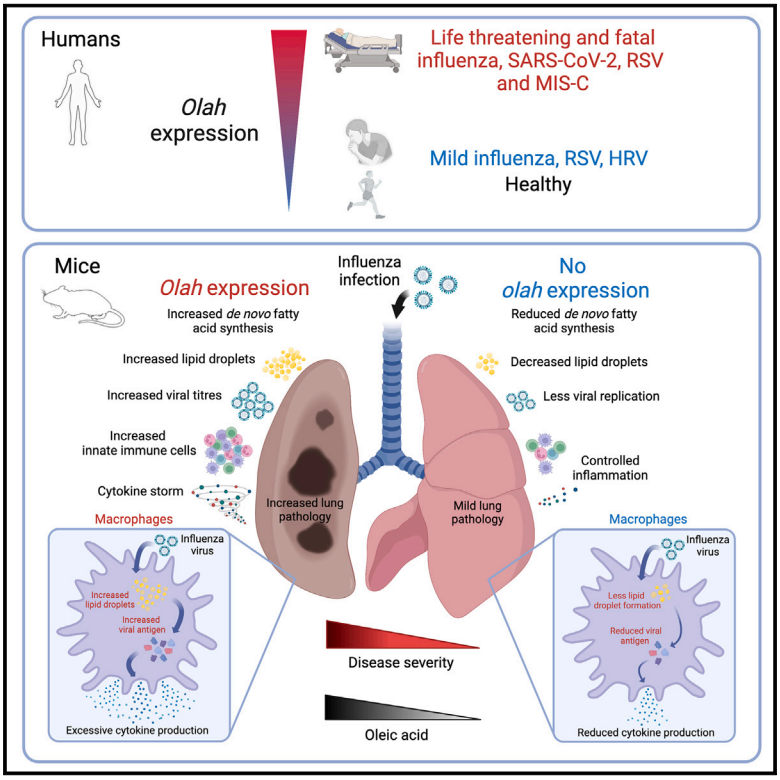

Highlights

- Fatal H7N9 flu patients express high *OLAH* levels throughout hospitalization
- High *OLAH* levels are detected in severe H1N1, COVID-19, RSV, and MIS-C patients
- *Olah*$^{-/-}$ mice are protected from lethal influenza disease and excessive inflammation
- *Olah* expression in macrophages drives viral infection and an inflammatory milieu

Authors

Xiaoxiao Jia, Jeremy Chase Crawford, Deborah Gebregzabher, ..., Zhongfang Wang, Brendon Y. Chua, Katherine Kedzierska

Correspondence

jeremy.crawford@stjude.org (J.C.C.), wangzhongfang@gird.cn (Z.W.), bychua@unimelb.edu.au (B.Y.C.), kkedz@unimelb.edu.au (K.K.)

In brief

High expression of an enzyme involved in fatty acid production, oleoyl-ACP hydrolase (OLAH), drives severe disease outcomes during respiratory infections.

Jia et al., 2024, Cell *187*, 4586–4604
August 22, 2024
https://doi.org/10.1016/j.cell.2024.07.026

CellPress

CellPress
OPEN ACCESS

Cell

Article

High expression of oleoyl-ACP hydrolase underpins life-threatening respiratory viral diseases

Xiaoxiao Jia,[1,30] Jeremy Chase Crawford,[2,3,30,*] Deborah Gebregzabher,[1] Ebony A. Monson,[4] Robert C. Mettelman,[2] Yanmin Wan,[5] Yanqin Ren,[6] Janet Chou,[7] Tanya Novak,[8] Hayley A. McQuilten,[1] Michele Clarke,[1] Annabell Bachem,[1] Isabelle J. Foo,[1] Svenja Fritzlar,[1] Julio Carrera Montoya,[1] Alice M. Trenerry,[1] Shuai Nie,[9] Michael G. Leeming,[9] Thi H.O. Nguyen,[1] Lukasz Kedzierski,[1] Dene R. Littler,[10] Andrew Kueh,[11,12,13,14] Tina Cardamone,[15] Chinn Yi Wong,[1] Luca Hensen,[1] Aira Cabug,[1] Jaime Gómez Laguna,[16] Mona Agrawal,[17] Tim Flerlage,[18] David F. Boyd,[19] Lee-Ann Van de Velde,[2] Jennifer R. Habel,[1] Liyen Loh,[1] Hui-Fern Koay,[1]

(Author list continued on next page)

[1]Department of Microbiology and Immunology, University of Melbourne, Peter Doherty Institute for Infection and Immunity, Melbourne, VIC 3000, Australia
[2]Department of Host-Microbe Interactions, St. Jude Children's Research Hospital, Memphis, TN 38105, USA
[3]Center for Infectious Diseases Research, St. Jude Children's Research Hospital, Memphis, TN 38105, USA
[4]Department of Microbiology, Anatomy, Physiology and Pharmacology, La Trobe Institute for Molecular Science, La Trobe University, Bundoora, VIC 3086, Australia
[5]Shanghai Public Health Clinical Centre and Institutes of Biomedical Sciences, Key Laboratory of Medical Molecular Virology of Ministry of Education/Health, Shanghai Medical College, Fudan University, Shanghai 201508, China
[6]Shanghai Public Health Clinical Centre, Fudan University, Shanghai 201508, China
[7]Division of Immunology, Boston Children's Hospital, Harvard Medical School, Boston, MA 02115, USA
[8]Department of Anesthesiology, Critical Care, and Pain Medicine, Boston Children's Hospital and Department of Anaesthesia, Harvard Medical School, Boston, MA 02115, USA
[9]Melbourne Mass Spectrometry and Proteomics Facility, Bio21 Molecular Science and Biotechnology Institute, University of Melbourne, Parkville, VIC 3052, Australia
[10]Infection and Immunity Program, Department of Biochemistry and Molecular Biology, Biomedicine Discovery Institute, Monash University, Clayton, VIC 3800, Australia
[11]Walter Eliza Hall Institute of Medical Research, Parkville, VIC 3052, Australia
[12]Department of Medical Biology, University of Melbourne, Parkville, VIC 3010, Australia
[13]Olivia Newton-John Cancer Research Institute, Heidelberg, VIC 3084, Australia

(Affiliations continued on next page)

SUMMARY

Respiratory infections cause significant morbidity and mortality, yet it is unclear why some individuals succumb to severe disease. In patients hospitalized with avian A(H7N9) influenza, we investigated early drivers underpinning fatal disease. Transcriptomics strongly linked oleoyl-acyl-carrier-protein (ACP) hydrolase (OLAH), an enzyme mediating fatty acid production, with fatal A(H7N9) early after hospital admission, persisting until death. Recovered patients had low *OLAH* expression throughout hospitalization. High *OLAH* levels were also detected in patients hospitalized with life-threatening seasonal influenza, COVID-19, respiratory syncytial virus (RSV), and multisystem inflammatory syndrome in children (MIS-C) but not during mild disease. In *olah*$^{-/-}$ mice, lethal influenza infection led to survival and mild disease as well as reduced lung viral loads, tissue damage, infection-driven pulmonary cell infiltration, and inflammation. This was underpinned by differential lipid droplet dynamics as well as reduced viral replication and virus-induced inflammation in macrophages. Supplementation of oleic acid, the main product of OLAH, increased influenza replication in macrophages and their inflammatory potential. Our findings define how the expression of OLAH drives life-threatening viral disease.

INTRODUCTION

Respiratory infections cause profound morbidity and mortality and remain the deadliest communicable disease.[1] However, it remains unclear why some individuals succumb to life-threatening disease while others develop mild symptoms. Severe influenza disease stems from over-activation and/or perturbation of immune responses, lung tissue damage, and hypercytokinemia.[2,3] Young children, elderly, pregnant women, individuals with comorbidities, and indigenous people are at high risk of severe

CellPress
OPEN ACCESS

Carolien E. van de Sandt,[1] Igor E. Konstantinov,[20] Stuart P. Berzins,[1,21] Katie L. Flanagan,[22,23,24] Linda M. Wakim,[1] Marco J. Herold,[11,12,13,14] Amanda M. Green,[3,18] Heather S. Smallwood,[17] Jamie Rossjohn,[10,25] Ryan S. Thwaites,[26] Christopher Chiu,[27] Nichollas E. Scott,[1] Jason M. Mackenzie,[1] Sammy Bedoui,[1] Patrick C. Reading,[1] Sarah L. Londrigan,[1] Karla J. Helbig,[4] Adrienne G. Randolph,[8,28] Paul G. Thomas,[2,3,28] Jianqing Xu,[5] Zhongfang Wang,[1,29,31,*] Brendon Y. Chua,[1,31,*] and Katherine Kedzierska[1,28,31,32,*]

[14]School of Cancer Medicine, La Trobe University, Bundoora, VIC 3086, Australia
[15]Department of Anatomy and Physiology, University of Melbourne, Parkville, VIC 3010, Australia
[16]Department of Anatomy and Comparative Pathology and Toxicology, Pathology and Immunology Group, University of Córdoba, International Excellence Agrifood Campus "CeiA3", 14014 Córdoba, Spain
[17]Department of Pediatrics, University of Tennessee Health Science Center, Memphis, TN 38163, USA
[18]Department of Infectious Diseases, St. Jude Children's Research Hospital, Memphis, TN 38105, USA
[19]Department of Molecular, Cell & Developmental Biology, University of California, Santa Cruz, Santa Cruz, CA 95064, USA
[20]Department of Cardiothoracic Surgery, Royal Children's Hospital, University of Melbourne, Melbourne Centre for Cardiovascular Genomics and Regenerative Medicine, Parkville, VIC 3052, Australia
[21]Institute of Innovation, Science and Sustainability, Federation University Australia, Ballarat, VIC 3353, Australia
[22]School of Health Sciences and School of Medicine, University of Tasmania, Launceston, TAS 7248, Australia
[23]School of Health and Biomedical Science, RMIT University, Bundoora, VIC 3083, Australia
[24]Tasmanian Vaccine Trial Centre, Clifford Craig Foundation, Launceston General Hospital, Launceston, TAS 7250, Australia
[25]Institute of Infection and Immunity, School of Medicine, Cardiff University, Heath Park, Cardiff, UK
[26]National Heart and Lung Institute, Imperial College London, London SW7 2AZ, UK
[27]Department of Infectious Disease, Imperial College London, London, UK
[28]Center for Influenza Disease and Emergence Response (CIDER), Athens, GA, USA
[29]State Key Laboratory of Respiratory Disease & National Clinical Research Center for Respiratory Disease, Guangzhou Institute of Respiratory Health, Guangzhou Medical University, Guangzhou, China
[30]These authors contributed equally
[31]These authors contributed equally
[32]Lead contact
*Correspondence: jeremy.crawford@stjude.org (J.C.C.), wangzhongfang@gird.cn (Z.W.), bychua@unimelb.edu.au (B.Y.C.), kkedz@unimelb.edu.au (K.K.)
https://doi.org/10.1016/j.cell.2024.07.026

disease.[4] Hospital admissions can also occur in previously healthy individuals with no prior risk factors. Among patients hospitalized with influenza-like illness during 2015–2016, >60% were previously healthy with no underlying conditions.[5] Factors driving severe influenza disease are of key importance if we are to design effective vaccines and therapies to control respiratory disease.

Increased susceptibility to severe influenza disease is multifactorial, and apart from impaired or overactive immune responses and/or minimal preexisting immunity,[6–9] host factors contribute to disease outcomes. Interferon-induced transmembrane protein-3 (IFITM3) can restrict virus replication by preventing endocytosed virus from entering the cytoplasm. However, single IFITM3 nucleotide polymorphisms can abrogate its function, leading to enhanced disease severity.[8,10–12] Mutations of genes associated with Toll-like receptor 3[13] and regulatory elements mediating interferon type I and type III production[14,15] increase susceptibility to severe influenza. Regulation of host lipid factors and their metabolism also impact influenza virus replication, inflammation, and disease outcome. Viral infections can drive lipidomic changes in lungs, typified by increased fatty acids and lipid mediators that provide energy and resources for virion assembly[16] and contribute to immune responses.[17–19]

Following the 2013 outbreak of the avian A(H7N9) influenza virus in China, with ~35% mortality rates, we defined immunity in fatal A(H7N9) disease.[11,20,21] Patients hospitalized with fatal A(H7N9) had dysregulated immune responses and hypercytokinemia in contrast to patients who recovered.[11,20] Here, we investigated mechanisms associated with hypercytokinemia and fatal disease. We identified a gene encoding for an enzyme involved in endogenous fatty acid production, oleoyl-acyl-carrier-protein (ACP) hydrolase (OLAH), as an early driver of fatal outcomes during A(H7N9). OLAH levels were associated with life-threatening seasonal influenza virus, severe acute respiratory syndrome coronavirus 2 (SARS-CoV-2), respiratory syncytial virus (RSV) infection, and multisystem inflammatory syndrome in children (MIS-C). OLAH regulates lipogenesis by catalyzing the release of fatty acids from an acyl-carrier protein following carbon chain elongation within the fatty acid synthase complex.[22] While OLAH liberates fatty acids of varying chain lengths, it has a high catalytic efficiency for oleoyl-ACP[23] to produce oleic acid.

To date, the role of OLAH in modulating immunity and driving disease outcomes has not been investigated for any disease. We found that *OLAH* gene expression in A(H7N9) patients with fatal disease is substantially elevated during early disease and remains high until death. High *OLAH* levels were found in four additional cohorts of patients hospitalized with life-threatening seasonal influenza, COVID-19, RSV infection, and in pediatric patients hospitalized with MIS-C. A CRISPR-Cas9-mediated gene knockout of *olah* in mice unraveled mechanisms underpinning OLAH-mediated disease severity. Infection of $olah^{-/-}$ mice with a lethal dose of influenza virus led to survival, mild disease, reduced lung viral loads, tissue damage, infection-driven pulmonary innate cell infiltration, and inflammation. This was associated with differential lipid droplet dynamics, reduced viral infection in macrophages, and inflammatory milieu. Inhibition of lipid droplet formation reduced viral infection in macrophages, while supplementation of oleic acid, OLAH's main product, increased influenza virus infection in macrophages and inflammation. Our

findings provide mechanistic insights into how the expression of OLAH drives life-threatening respiratory disease.

RESULTS

High expression levels of *OLAH* during early avian A(H7N9) influenza predict fatal disease outcomes

As avian influenza A(H7N9) virus leads to severe influenza disease with ~35% morbidity rates,[24,25] we investigated early biomarkers of fatal outcomes. To identify molecular signatures associated with fatal disease, we performed blood transcriptomics using our cohort of hospitalized H7N9 patients at Shanghai Public Health Clinical Centre.[11,20] Affymetrix Human Gene ST-2.0 arrays were performed on 8 H7N9 patients, 4 who recovered (mean age of 69) and 4 with fatal disease (mean age of 70) (Table S1). Patients who recovered (a9, a20, a73, and a134) were discharged within 14–23 days after disease onset, while fatal outcomes occurred at 19 days (patient a118) or after prolonged hospital stays on days 64, 70, and 76 (patients a131, a33, and a22) (Figure 1A). Plasma cytokine levels at 1–2 days following hospital admission showed that patients who died had higher inflammation compared with patients who recovered ($p = 0.028$; Figure 1B; data for the entire cohort in Wang et al.[11]), indicative of early hypercytokinemia preceding severe outcomes. Transcriptomics, performed on patients' blood collected within 6 days of hospital admission, identified differential expression of 10 genes defined by 16 probe sets, with 7 probe sets specific for one gene, *OLAH*, expressed at ~82-fold higher levels in patients who died compared with patients who recovered ($p < 0.001$; Figure 1C). High *OLAH* levels in fatal H7N9 patients were detected early after hospital admission and persisted until patients died, while patients who recovered exhibited low *OLAH* expression throughout hospital stays (Figure 1D). These analyses defined *OLAH* as the main differentially expressed gene during fatal A(H7N9) disease.

High *OLAH* expression is linked to life-threatening seasonal influenza, SARS-CoV-2, and RSV infections

Given scarce data on *OLAH* expression in humans, we analyzed mRNA levels across tissues and peripheral blood mononuclear cells (PBMCs) in healthy adults. High *OLAH* levels were found in lungs, spleens, T cells, monocytes, and remaining PBMC populations (Figure 1E). Detectable *OLAH* levels were detected in thymus and tonsil tissues. Within lungs, the site of influenza virus infection, *OLAH* expression was predominantly detected in $CD14^+$ monocytes (Figure 1F).

To investigate *OLAH* expression in patients hospitalized with seasonal influenza, we utilized a patient cohort with single-cell RNA sequencing (scRNA-seq) data performed using PBMCs collected at 1–14 days after hospital admission.[26] This cohort consisted of 2 healthy participants and 3 intensive care unit (ICU) patients hospitalized with influenza A(H1N1) or influenza B virus requiring mechanical ventilation. Our findings showed elevated *OLAH* expression in ICU influenza patients but not among healthy individuals (Figure 1G), predominantly within monocytes/macrophages. Accordingly, *in vitro* infection of PBMCs from healthy individuals with A/California/07/2009 led to increased intracellular nucleoprotein (NP) levels in monocytes, demonstrating their susceptibility to influenza virus infection (Figure 1H).

To determine whether the observed association between *OLAH* levels and acute viral infection-related illness severity extended beyond influenza, we evaluated gene expression profiles in patients hospitalized with COVID-19 or pediatric acute respiratory disease (pARDS). Bulk RNA-seq analysis of blood from infants, children, or young adults (aged 0–21) with SARS-CoV-2 (Tables S2 and S3) identified *OLAH* as the single most differentially expressed gene increased in patients hospitalized with life-threatening respiratory dysfunction compared with those hospitalized with no to minimal respiratory dysfunction (Figure 2A). When compared with healthy individuals, *OLAH* expression was minimally elevated in hospitalized COVID-19 patients with no to minimal respiratory dysfunction (Figure 2A; $p = 0.08$). Conversely, increased *OLAH* expression was detected in patients with moderate-to-severe ($p = 0.01$) and life-threatening respiratory dysfunction ($p < 0.001$). Patients hospitalized with MIS-C, a post-infection severe hyperinflammatory complication temporally related to prior SARS-CoV-2 infection, showed even further elevation in *OLAH* levels compared with patients with moderate-to-severe disease ($p < 0.05$). We found no significant associations between *OLAH* and BMI, age, or sex (Figures S1A–S1D). Visualizing *OLAH* expression as a function of time (days between symptom onset and sample collection) demonstrated an increase in *OLAH* expression from early time points after infection (~day 5) among patients with severe disease, with a peak in *OLAH* at ~9 days after symptom onset, conversely to minimal *OLAH* expression in patients with minimal disease severity (Figure 2B).

To investigate downstream consequences of differential *OLAH* expression in patients with severe respiratory disease, we performed *a priori* analysis of oleic acid abundance in an independent cohort of patients diagnosed with COVID-19 (Table S4). HPLC was used to assay plasma lipid abundances. Oleic acid (C18:1) was identified based on retention time, *m/z*, and fragment data. After controlling for potential effects of sex, age, and race, oleic acid abundance was significantly higher among hospitalized patients than those who remained ambulatory ($p < 0.05$; Figure 2C).

In our fourth disease cohort, we interrogated scRNA-seq data of tracheal aspirate samples obtained from children hospitalized with acute respiratory failure requiring endotracheal intubation secondary to known or suspected lower respiratory tract infection (LRTI) or for an etiology unrelated to lung injury (e.g., head injury neurologic failure; control patients).[28] As with severe influenza, *OLAH* expression was elevated among monocytes/macrophages and neutrophils in patients with mild and moderate/severe pARDS, particularly in confirmed RSV infections (Figure 2D). When grouped by respiratory disease severity, *OLAH* expression was increased in proportion to the severity of pARDS experienced (Figure 2E). Elevated *OLAH* expression was detected in patients without pARDS who were intubated due to severe disease caused by an LRTI and acute lung failure. *OLAH* levels in patients without LRTI and control patients intubated because of neurologic failure without lung disease were negligible, indicating a strong link between *OLAH* expression and respiratory viral infection but not to unrelated non-respiratory injuries.

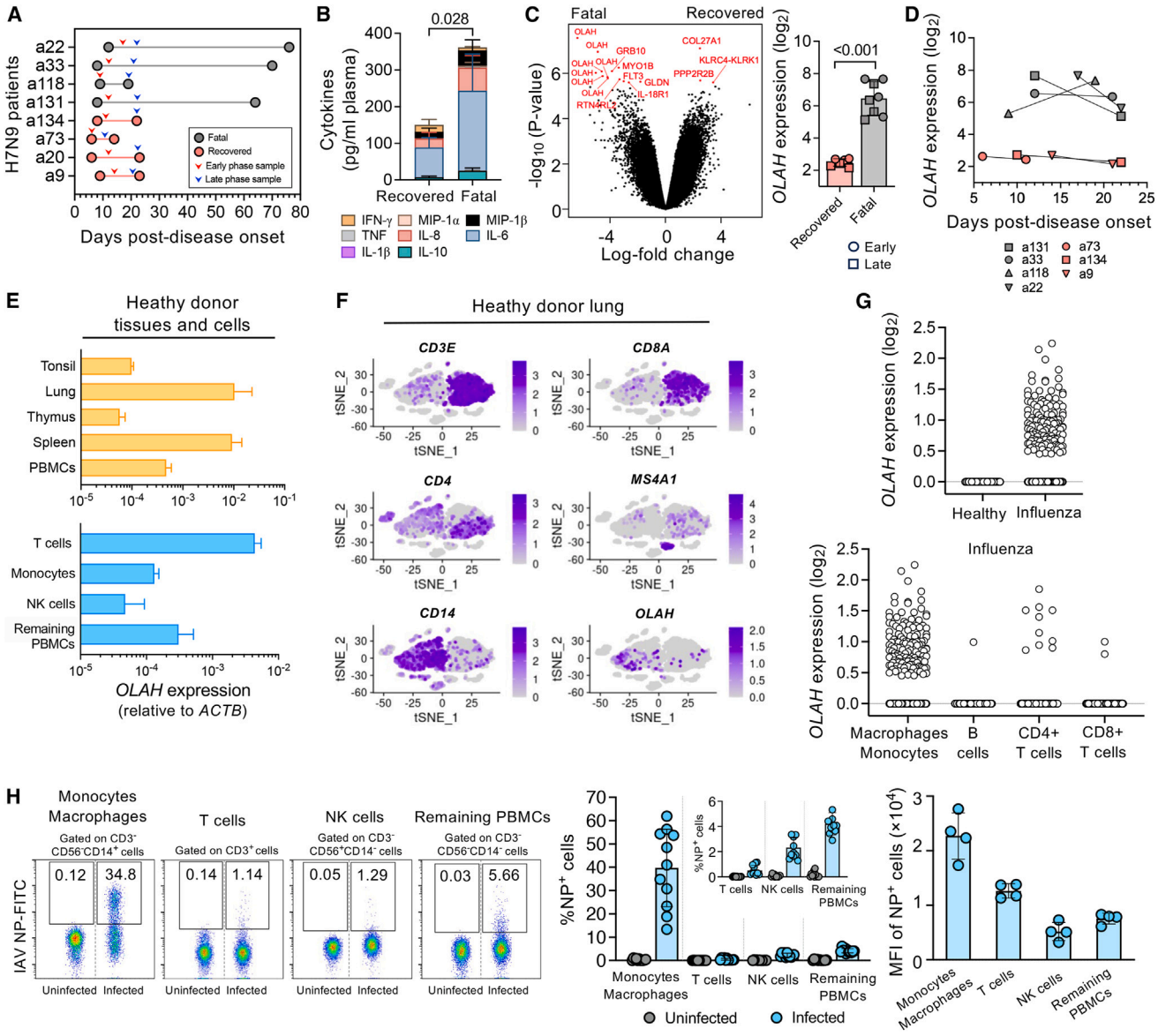

Figure 1. Elevated *OLAH* expression in humans is associated with life-threatening influenza disease outcomes

(A) Timeline of hospital stay of H7N9-infected patients who recovered or died. Circles denote admission and discharge/death days post-disease onset. Arrows indicate early and late blood samples for microarray-based transcriptomic analysis.

(B) Plasma cytokines (mean ± SD) were assessed within 1–2 days of admission, and cytokine data reported as a larger cohort in Wang et al.[11]).

(C) Volcano plot showing differential gene probeset expression between recovery and fatal patients at early disease time points. *OLAH* expression levels (mean ± SD) in early (circles) and late (squares) samples with paired data.

(D) *OLAH* transcript expression in paired early and late samples.

(E) qPCR was performed on RNA from single-cell suspensions of healthy human tissues and PBMCs for *OLAH* transcript levels (n = 2–3/sample). Bar graphs depict average expression levels (±SD) relative to house-keeping gene actin.

(F) t-distributed stochastic neighbor embedding representation of single-cell RNA expression from healthy human lungs showing *OLAH* expression and association with genes used for cell-type annotations.

(G) *OLAH* expression in single-cell RNA transcriptomic data acquired from PBMCs of healthy individuals (n = 2) or patients hospitalized with influenza (n = 3) at 1–14 days post-symptom onset.[26] Expression levels are segregated by disease state and cell population.

(H) PBMCs from healthy donors (n = 11) were uninfected or infected with A/California/07/2009 at MOI = 4; intracellular nucleoprotein (NP) expression analyzed. Representative concatenated dot plots showing percentages of cells expressing NP from infected or uninfected cultures. Bar graphs show mean frequencies (±SD) of cells expressing NP (n = 11) and representative MFI (±SD) from 4 donors.

Statistical analysis was performed using Mann-Whitney test.

See also Figure S7.

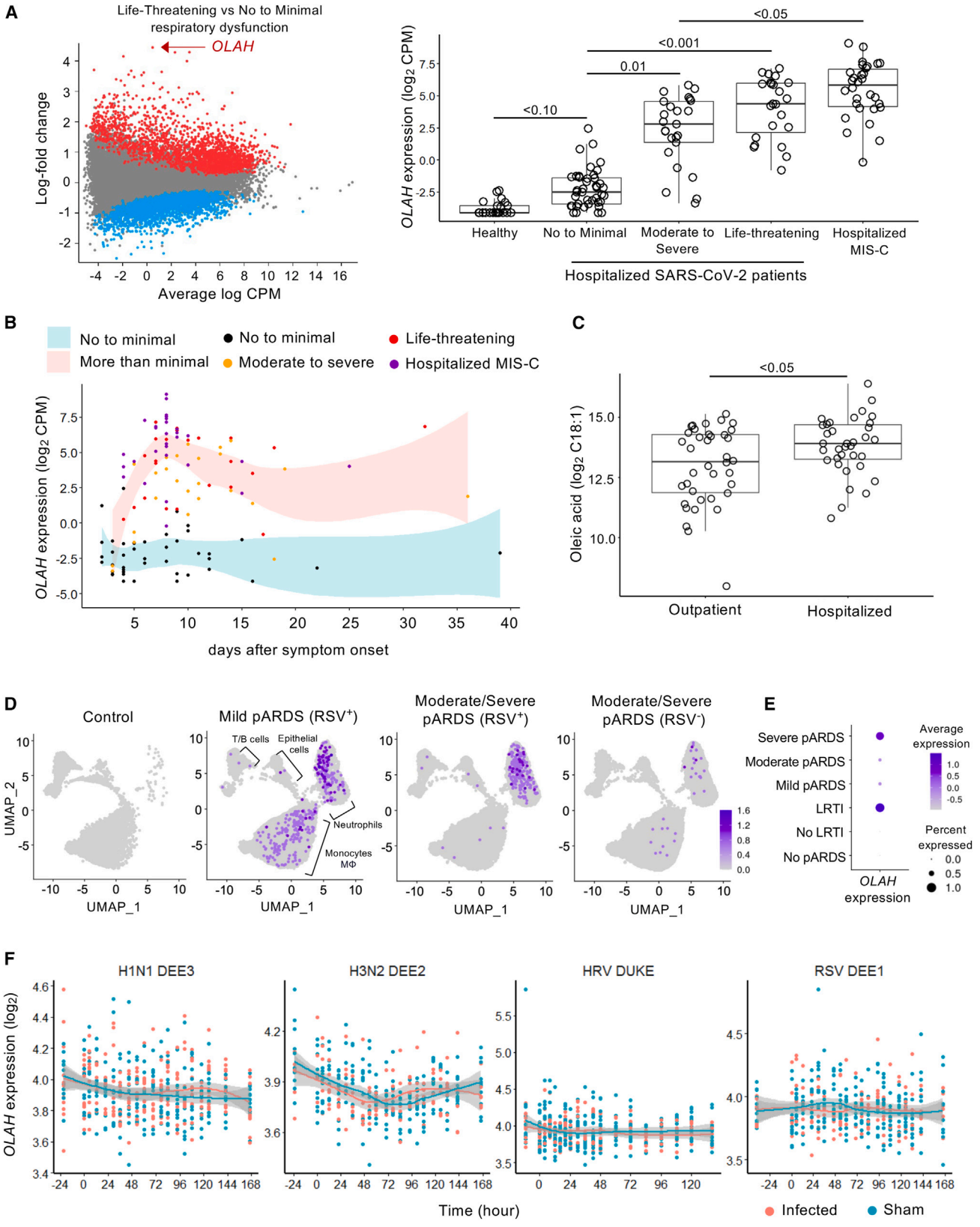

(legend on next page)

To understand *OLAH* expression among healthy individuals and those with mild respiratory infections, we analyzed blood microarray expression data from human challenge models of infections with H1N1 (2 studies), H3N2 (2 studies), human rhinovirus virus (HRV) (2 studies), and RSV (1 study) spanning 38 h prior to infection to 170 h post-infection.[29] We found no differences in *OLAH* expression following sham infection and mild infection across these datasets (Figures 2F and S1E). Significant effects of time on *OLAH* expression were observed in three of human challenge studies, but these slight changes in *OLAH* were consistent regardless of infection status, suggesting technical rather than biological variation. *OLAH* expression from human samples obtained up to 7 days after challenge exhibited no differences between sham and mild infection. Additionally, bulk RNA-seq from nasal curettage cells obtained after controlled human RSV infection[30] showed no variation in *OLAH* expression across participants who became actively infected with or without symptoms or those not exhibiting active viral replication (Figure S1F).

Overall, our data introduce the concept that highly elevated *OLAH* expression in adults and children underpins severity of human viral infections caused by influenza viruses, RSV and SARS-CoV-2, and life-threatening post-infectious hyperinflammatory MIS-C. The consistently low *OLAH* levels observed among healthy individuals and during mild infections from human challenge suggest that OLAH is specific to severe disease and merits further investigation as a potential target for novel therapeutics.

OLAH-mediated lipogenesis is attenuated in *olah*$^{-/-}$ mice

As our findings linked *OLAH* expression with severe influenza disease in humans, we investigated OLAH's role in driving severe influenza in a mouse model. We analyzed *olah* mRNA expression across organs and tissues in naive wild-type (WT) C57BL/6 mice. The highest levels of *olah* mRNA were detected in testis, placenta, brain, lung, and thymus, and, to a lesser extent, in liver, spleen, and lymph nodes (Figure 3A). Within lungs, higher expression of *olah* was detected in non-hematopoietic CD45^{-} cells compared with hematopoietic CD45^{+} immune cells (p = 0.014; Figure 3B). To generate *olah*-deficient (*olah*$^{-/-}$) C57BL/6 mice, we performed CRISPR-Cas9-targeted deletion of exons 1 and 2 of the *olah* allele on chromosome 2 (Figure 3C). Successful deletion was confirmed by undetectable expression of the *olah* gene (Figure 3C). Comparative histological analysis of 28 tissue and organ sections from naive *olah*$^{-/-}$ and WT mice did not reveal any differences aside from early indications of urethral obstructive syndrome and mild hyperplasia in spleens of *olah*$^{-/-}$ mice (Table S5). Both *olah*$^{-/-}$ and WT mice were similar in outward appearance, body weights (Figure S2A), and immune cell frequencies within the lung, spleen, and thymus (Figure S2B).

Lipidomic analysis of lung tissues from naive *olah*$^{-/-}$ and WT mice showed differences in abundance of cardiolipins and lysophosphatidylethanolamines at the class level (Figure S2C). At the species level, 69 distinct lipids were decreased in *olah*$^{-/-}$ mice; 13 were upregulated (Figures 3D and 3E). Of those downregulated, ~25% were cardiolipins, containing abundant OLAH catalytic products and their derivatives (Figure 3F).[31,32] Additionally, ~37% were lysophosphatidylethanolamines, phospholipids implicated in intracellular signaling and innate response induction.[33]

Examining fatty acids produced by OLAH, we detected reduced amounts of oleic (p = 0.033), palmitoleic (p = 0.035), palmitic (p = 0.019), and myristic acid ($p \leq 0.001$) in *olah*$^{-/-}$ mice, while levels of stearic acid and lauric acid, the latter a fatty acid not produced by OLAH, remained unaltered (Figure 3G). The lack of difference in stearic acid levels between WT and *olah*$^{-/-}$ mice may be attributed to the preferential cleavage of oleoyl-ACP intermediates by OLAH at the expense of stearic acid production. Our data indicate that the genetic deletion of *olah* results in functional impacts on OLAH-mediated lipogenesis, shown by decreased fatty acid synthesis and levels of related lipid species.

Olah deficiency protects from severe influenza

To determine the impact of OLAH on influenza outcomes, we infected *olah*$^{-/-}$ and WT mice intranasally (i.n.) with 2 different doses of A/HKx31 (H3N2; X31) influenza strain corresponding to lethal (10^5 plaque-forming units [PFU]) and non-lethal (10^4 PFU) infection (Figure 4A). To elucidate effects of OLAH on disease severity, we examined the body weight loss and survival

Figure 2. *OLAH* expression is elevated during severe respiratory infection and MIS-C but not among healthy participants or mild infections

(A) Bulk RNA-seq was performed on blood from hospitalized COVID-19 patients <21 years (n = 143). MD plot of differentially expressed genes between hospitalized patients with no/minimal respiratory dysfunction (blue) and hospitalized patients experiencing life-threatening fatal respiratory failure (red). *OLAH* expression in healthy, non-infected individuals (n = 22) and hospitalized SARS-CoV-2 patients grouped by disease severity (hospitalized with no/minimal respiratory dysfunction, n = 43; hospitalized with moderate/severe respiratory dysfunction, n = 25; hospitalized with life-threatening respiratory dysfunction, n = 23; and hospitalized/diagnosed with MIS-C[27] (n = 30). p values were obtained from a model controlling for days since symptoms onset, sex, whether a patient was previously healthy, steroid administration prior to sampling, bacterial co-infection, age, race, and ethnicity; adjusted for multiple comparisons.

(B) *OLAH* expression from (A) plotted across time. Curves were fit using the LOESS function with default parameters.

(C) Log_2 oleic acid abundances from SARS-CoV-2-positive patients as outpatients (n = 38) or hospitalized (n = 35). Significance was assessed using analysis of variance while controlling for age, sex, and race.

(D) *OLAH* expression in single-cell RNA transcriptomic data acquired from tracheal aspirate samples of RSV-infected children with no/mild (n = 5) or moderate/severe pediatric ARDS (pARDS) (n = 7), non-RSV-related infection but with moderate/severe pARDS (n = 5), and control children without acute lower respiratory tract infection or lung injury (n = 6).

(E) *OLAH* expression in children grouped by pARDS severity and lower respiratory tract infection (LRTI) status.

(F) *OLAH* expression across time for four human challenge models of mild respiratory infections (H1N1-DEE3, n = 477; H3N2-DEE2, n = 355; HRV-Duke, n = 471; and RSV-DEE4, n = 420).

Smooth curves are fit using a locally estimated scatterplot smoothing (LOESS) model, with red depicting samples from infected participants; blue showing samples from sham-infected participants. Linear mixed models were used to test for effects of time, infection status, and interaction of time with infection status, with participants included as a random effect. Infection status was not significant for any study. Time was statistically significant for studies H1N1-DEE3 ($p < 0.001$) and H3N2-DEE2 ($p < 0.001$).

See also Figure S1.

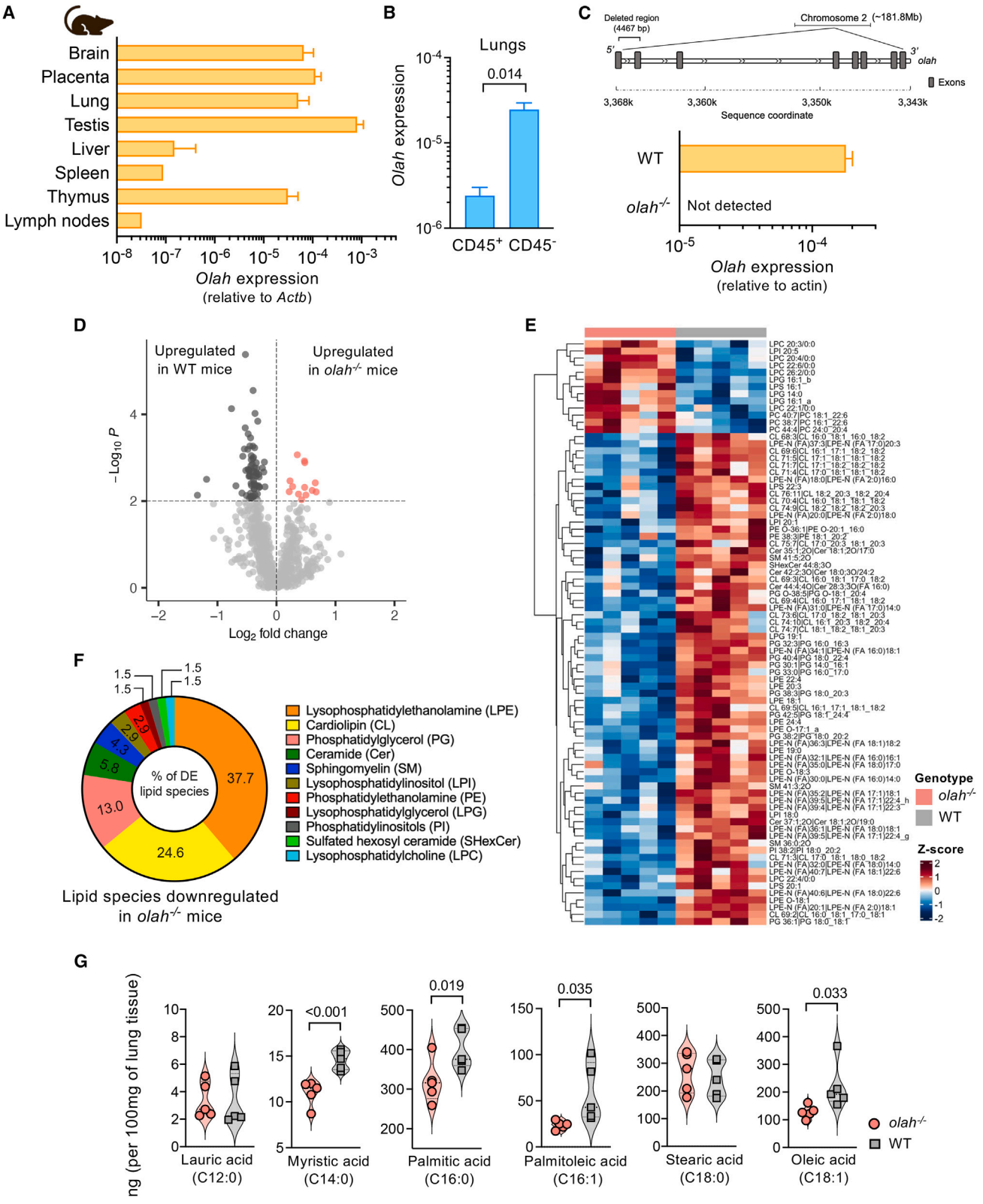

(legend on next page)

of *olah*$^{-/-}$ and WT mice following infection. Animals infected with the 10^4 PFU dose survived (Figure 4B); however, *olah*$^{-/-}$ mice lost significantly less body weight comparing to WT mice over 10 days (Figure 4C) ($p < 0.05$ on days 4, 6, and 8); confirmed by area under the curve (AUC) profiles ($p = 0.009$). Differences in disease outcomes were striking following infection with the lethal 10^5 PFU dose. While influenza-infected *olah*$^{-/-}$ mice survived, ~50% of WT mice succumbed to disease ($p = 0.021$; referred to as LD_{50} infection; Figure 4B). Infection in WT mice exhibited more body weight losses during disease, particularly at days 5–8 post-infection ($p < 0.05$); shown by cumulative AUC comparisons ($p = 0.008$; Figure 4C). Pooled data from 5 experiments ($n = 42$ WT; 28 *olah*$^{-/-}$ mice) showed that protection against lethality in *olah*$^{-/-}$ mice was not sex-specific, with survival rates of male and female *olah*$^{-/-}$ mice being equivalent (>93%), compared with ~50% of sex-matched WT mice (males $p = 0.005$; females $p = 0.016$; Figure 4D).

Histopathological analysis of lung sections from LD_{50}-infected WT mice indicated the presence of moderate-to-severe pulmonary pathology as early as day 1 post-infection (Figure 4E; Table S6). Observations included acute necrotizing bronchitis, respiratory epithelium disruption accompanied by multifocal lymphocytic infiltration of the interstitium and vasculitis, and areas of high-protein edema suggestive of viral pneumonia. Conversely, these were milder and less consistent in *olah*$^{-/-}$ mice, reflected in lower percentages of damage and lesions in tissue sections from *olah*$^{-/-}$ mice across 5 days post-infection ($p = 0.013$; days 3 and 5 $p < 0.001$; Figure 4F), indicating less severe pulmonary pathology in *olah*$^{-/-}$ mice.

Our results provide evidence that OLAH drives severe influenza disease in mice, both with respect to morbidity and mortality, supporting our observations in H7N9 patients linking high *OLAH* levels with fatal outcomes.

Absence of *olah* reduces pulmonary viral-induced inflammation and lipid droplet formation

To investigate mechanisms underpinning OLAH-mediated influenza severity, we analyzed inflammatory responses in LD_{50}-infected *olah*$^{-/-}$ and WT mice. Pro-inflammatory cytokines in lungs and bronchoalveolar lavage (BAL) of *olah*$^{-/-}$ mice were reduced compared with WT mice, particularly at day 1 post-infection ($p = 0.031$; Figure 4G), with lower levels of tumor necrosis factor (TNF), MIP-1α, and MIP-1β in both BAL (TNF, MIP-1α, $p = 0.008$; MIP-1β, $p = 0.031$) and lungs ($p = 0.008$; Figure S3A). Decrease in pro-inflammatory cytokines was commensurate with decreased cell numbers at the infection site, most evident at day 1 (BAL, $p = 0.01$; lungs, $p = 0.005$; Figure S3B). Particularly, lungs of *olah*$^{-/-}$ mice had reduced numbers of alveolar ($p = 0.007$) and interstitial macrophages ($p \leq 0.001$), neutrophils ($p \leq 0.001$), $\gamma\delta$ T cells ($p = 0.005$), natural killer (NK) ($p = 0.003$), and natural killer T cells ($p = 0.011$; Figure 4H). These differences were not evident at days 2 or 3 (Figure S3C). Higher numbers of macrophages and epithelial cells expressing intracellular NP were detected in lungs of infected WT mice at days 1 post-infection (Figure 5A), suggesting their involvement in exacerbating OLAH-mediated disease. Within NP$^+$ lung populations in WT and *olah*$^{-/-}$ mice, ~50%–60% of epithelial cells and ~10%–20% of neutrophils also expressed hemagglutinin (HA) and were defined as productively infected[34] Figure S3D). ~10% of macrophages were productively infected at day 1. The infection increased to ~50% after 3 days.

LD_{50} infection of WT and *olah*$^{-/-}$ mice resulted in >74 differentially expressed lipid species in lungs on day 1 post-infection (Figure S2D). Higher amounts of phospholipids containing polyunsaturated fatty acids, known eicosanoid precursors, were upregulated in infected WT mice, including those associated with arachidonic acid (20:4), dihomo-γ-linolenic acid (20:3), and adrenic acid (22:4) (Figure S2E), indicating a role for lipid mediators in driving OLAH-mediated inflammation during infection. Hence, we provide evidence that severe OLAH-mediated disease is underpinned by inflammatory responses reminiscent of early hypercytokinemia observed during fatal H7N9 infection in humans during early infection (Figure 1B). Without OLAH, the early onset of hypercytokinemia was averted.

To determine the role of immune and non-immune cells in driving OLAH-mediated disease, we generated bone marrow (BM) chimeras using *olah*$^{-/-}$ and WT mice. Adoptive transfer of donor WT BM cells into irradiated *olah*$^{-/-}$ recipients (WT → *olah*$^{-/-}$) provided a model with only hematopoietic-derived immune cells expressing *olah*. In the *olah*$^{-/-}$ → WT scenario, only non-immune cells express *olah* (Figures 5B and S4A). We also established controls where donor WT or *olah*$^{-/-}$ BM cells were transferred into the same recipient strains (WT → WT; *olah*$^{-/-}$ → *olah*$^{-/-}$). Following LD_{50} infection, 90% of recipients with WT BM cells (WT → *olah*$^{-/-}$ and WT → WT) succumbed to disease within 7 days, whereas 60% of mice with *olah*$^{-/-}$ BM (*olah*$^{-/-}$ → WT and *olah*$^{-/-}$ → *olah*$^{-/-}$; $p \leq 0.001$) survived (Figure 5C). WT BM-recipients also experienced more body weight loss (from day 3, $p < 0.05$, Figure 5C), implicating that

Figure 3. Deletion of *olah* in mice reduces *de novo* fatty acid synthesis

(A) qPCR measuring *olah* was performed on RNA from tissues or single-cell suspensions derived from organs ($n = 1$–6).

(B) Sorted CD45$^+$ and CD45$^-$ cells from lungs of naive C57BL/6 (WT) mice ($n = 3$). Bar graphs depict average expression (±SD) relative to expression of housekeeping actin gene.

(C) Schematics of the *olah* gene on mouse chromosome 2 and the region within exon 1 and 2 targeted for deletion. qPCR on RNA from WT and *olah*$^{-/-}$ mice confirm knockout of *olah*.

(D) Volcano plot showing differentially expressed lipid species in lungs of naive mice. Dark gray and red dots represent species upregulated (false discovery rate [FDR] < 0.01) in WT and *olah*$^{-/-}$ mice.

(E) Heatmap depicting levels of differentially expressed lipid species ($p < 0.01$) in lungs of naive WT and *olah*$^{-/-}$ mice. LPE 16:1(a) and LPE 16:1(b) are *sn* substitution isomers.

(F) Proportion of lipid species, typed by lipid class, downregulated in *olah*$^{-/-}$ mice.

(G) Fatty acids levels in lungs of naive mice ($n = 5$/group) catalyzed by OLAH, except lauric acid.

Statistical analysis was performed by Welch t test.

See also Figure S2.

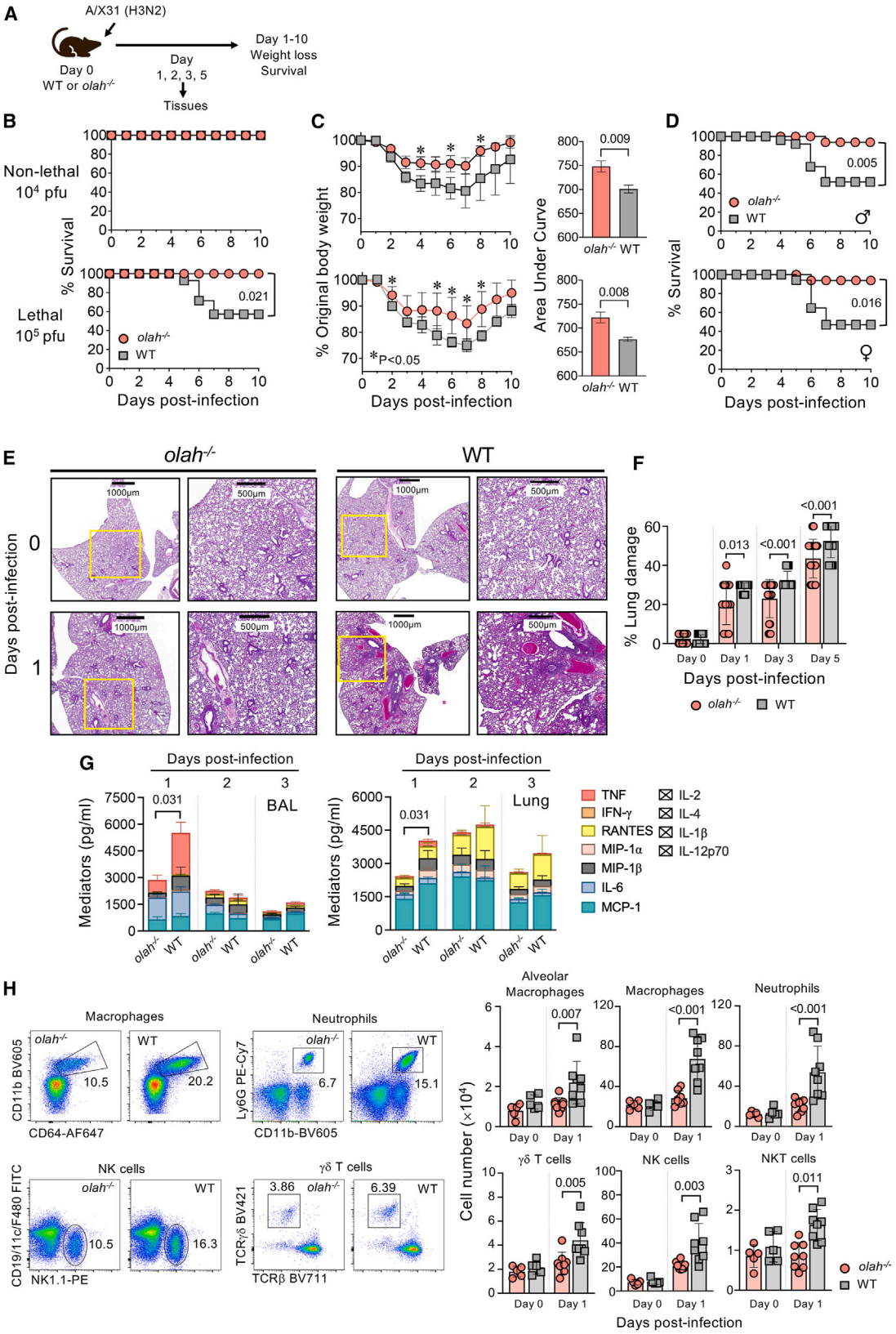

(legend on next page)

OLAH-expressing immune cells exacerbate disease severity. Analysis of donor-derived immune cells in lungs of influenza-infected recipients revealed lower numbers of *olah*$^{-/-}$ macrophages in *olah*$^{-/-}$ → WT mice compared with WT macrophages in WT → *olah*$^{-/-}$ mice (Figure 5D), linking *olah* expression in macrophages with disease outcomes.

Since lipid droplets play important roles in viral replication cytokine production,[17,35] and given the role of OLAH in lipogenesis, we investigated how OLAH affected lipid droplet formation in lungs following LD_{50} infection. Although higher numbers of lipid droplets were initially detected in lungs from naive *olah*$^{-/-}$ ($p < 0.001$) (Figures 5E, 5F, and S4B), they decreased at day 1 post-infection ($p < 0.001$) and were reduced for at least 3 days. Conversely, lipid droplet accumulation in WT mice increased after infection comparing to *olah*$^{-/-}$ mice (days 1–3; $p < 0.001$). CD36, the fatty acid scavenger receptor, and IAV-NP co-localized with concentrated regions of lipid droplets (Figure 5E). *Olah*$^{-/-}$ mice exhibited reduced lung viral titers compared with WT mice, especially at day 1 post-infection ($p < 0.001$) (Figure 5G), demonstrating that expression of OLAH promotes virus-induced lipid droplet formation in infected lungs.

Epitope-specific CD8$^+$ T cells are not affected by *olah*

To determine whether *olah* affected adaptive immunity, we analyzed influenza-specific T cells at day 10 post-LD_{50} infection (Figure S5A). Equivalent numbers of CD8$^+$ and CD4$^+$ T cells were detected in lungs and BAL of infected WT and *olah*$^{-/-}$ mice (Figure S5B). Although the majority of CD8$^+$ T cells exhibited effector phenotypes (CD62L$^-$CD44$^+$) (Figure S5C), their numbers did not differ between mice. The same occurred for T cell populations with naive (CD62L$^+$CD44$^-$) and memory (CD62L$^+$CD44$^+$) phenotypes. *olah*$^{-/-}$ and WT mice induced similar levels of influenza-specific CD8$^+$ T cells directed at immunodominant D^bNP_{366} and D^bPA_{224} epitopes (Figure S5D), with similar capacity of CD8$^+$ T cells from WT and *olah*$^{-/-}$ mice secreting cytokines (Figure S5E), indicating that OLAH does not impact T cell-mediated immunity.

Macrophages play an important role in driving OLAH-mediated disease severity

As our data in humans and mice demonstrated that macrophages were associated with severe influenza, we investigated how *olah* expression impacted virus infection of macrophages. We analyzed mitochondrial abundance and membrane potential, and glucose uptake in WT and *olah*$^{-/-}$ macrophages *in vivo* following LD_{50} infection using fluorescent metabolic dyes, MitoTracker, tetramethylrhodamine (TMRM), and 2-(7-nitro-2,1,3-benzoxadiazol-4-yl)-D-glucosamine (2-NBDG). Although mitochondrial abundance and glucose uptake increased over 3 days post-infection, *olah* expression had minimal effects on metabolic features (Figure S6A). Both WT and *olah*$^{-/-}$ macrophages exhibited similar M1-like phenotypes (iNOS^{high}, Arg-1^{low}, CD206^{low}) early after infection and acquired M2-like features (iNOS^{low}, Arg-1^{high}, CD206^{high}) at day 3 (Figure S6B), indicating unchanged phenotypic polarization.

We quantified viral mRNA encoding for NP and matrix (M) antigens in CD64$^+$F4/80$^+$ peritoneal macrophages from WT and *olah*$^{-/-}$ mice (Figure 6A) after *in vitro* infection.[36] In Madin Darby canine kidney (MDCK) cells, viral mRNA expression increased over time (Figure 6B). Although increases were observed in WT and *olah*$^{-/-}$ macrophages, expression levels were similar between groups, suggesting that OLAH may not modulate early stages of viral infection, viral entry, or viral mRNA production.

Increased viral mRNA in influenza-infected MDCKs was concomitant with intracellular expression of viral proteins and detected in ~65%–70% of cells at 8 h post-infection (Figure 6C). Despite similar viral mRNA levels, fewer *olah*$^{-/-}$ macrophages expressed viral proteins compared with WT macrophages (~2-fold; NP: $p = 0.022$; M: $p = 0.028$). Reduced expression of viral proteins in *olah*$^{-/-}$ macrophages was confirmed by proteomic analysis (Table S7). Differences in antigen expression occurred from 4 h post-infection (Figure 6D), reflected in the amount of viral antigen expressed (Figure S6C), indicating that *olah* expression in macrophages increased viral antigen production in male- and female-derived macrophages (Figure 6E). Infection of WT macrophages resulted in production of higher levels of inflammatory mediators TNF, MIP-1α, and MIP-1β (Figure 6F), reminiscent of the profiles observed in lungs and BAL of infected WT mice (Figure 4G).

To understand whether *olah*'s association with increased viral infection was limited to respiratory viruses, we investigated replication of West Nile Virus (WNV) and murine norovirus (MNV) in *olah*$^{-/-}$ macrophages. Viral titers of WNV, Kunjin virus (WNV_{KUN}) were significantly reduced (~2-fold) in culture supernatants of infected *olah*$^{-/-}$ compared with WT macrophages ($p = 0.047$; Figure 6G). No differences were observed following infection with MNV (Figure 6G), but this suggests that *olah* expression could also be involved in promoting flavivirus infections.

Oleic acid drives aberrant virus-induced responses in macrophages and exacerbates disease severity following influenza virus infection

As OLAH promoted virus-induced lipid droplets in lungs (Figures 5E and 5F), we analyzed lipid droplet usage in macrophages.

Figure 4. *Olah* drives influenza-virus-induced pulmonary inflammation and innate cell infiltration, lung damage, and fatal outcomes

(A–C) (A) Mice (6–9 weeks) were intranasally infected with A/X31 to establish mild (10^4 PFU; $n = 5$–6/group) or severe disease (10^5 PFU; LD_{50} infection; $n = 10$–14) and monitored for (B) survival and (C) body weight loss (mean ± SEM). Mice were culled at humane endpoint; ≥25% of original body weight lost. Body weights across time were quantified by area under the curve (mean ± SD).

(D) Survival rates of LD_{50}-infected male ($n = 25$ WT; $n = 16$ *olah*$^{-/-}$) and female ($n = 17$ WT; $n = 12$ *olah*$^{-/-}$) mice from 5 independent experiments.

(E) Representative hematoxylin and eosin-stained lung sections from mice following severe A/X31 infection.

(F) Lungs ($n = 2$/group/time point) were sliced (5 μm), and 5 sections were independently graded for tissue damage.

(G) Cytokine levels (mean ± SD) in bronchoalveolar lavage (BAL) and lungs of mice following LD_{50} infection. Crossed-out boxes indicate cytokines not detected.

(H) Representative dot plots (left) and numbers (mean ± SD) of innate cells at 1-day post-infection (right) relative to numbers in naive mice (day 0; Figure 3B).

Statistical analysis was performed by (B and D) Kaplan-Meier method, (C, G, and H) Mann-Whitney test, and (F) two-way ANOVA with a Holms-Sidak post hoc test. *$p < 0.05$.

See also Figures S2, S3, S5, and S7.

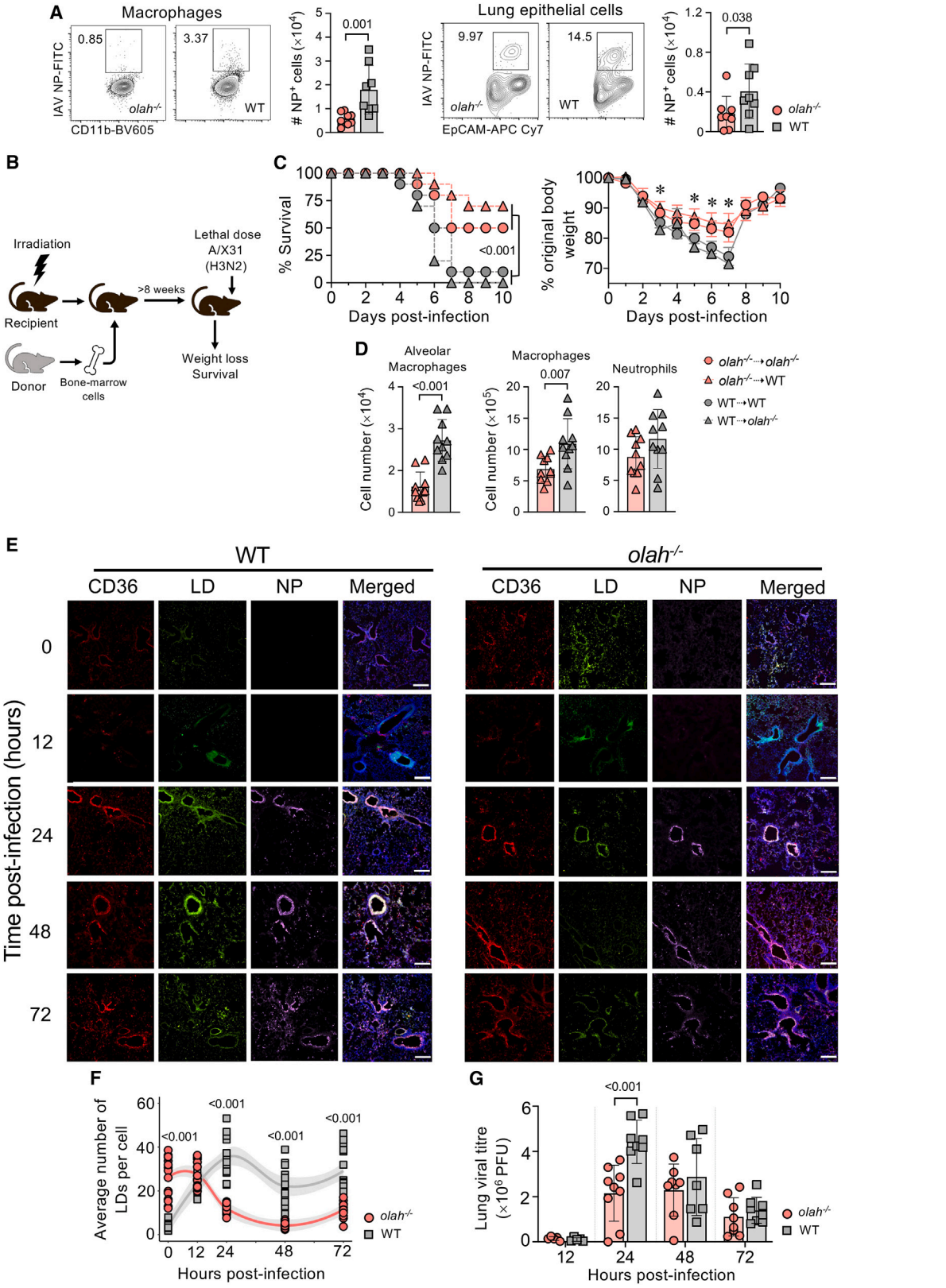

(legend on next page)

Higher numbers of lipid droplets were initially detected in *olah*$^{-/-}$ compared with WT macrophages prior and during early infection (Figures 7A and S4C). However, while viral infection increased lipid droplets in *olah*$^{-/-}$ macrophages over 8 h by 3-fold, a more substantial increase of >20-fold occurred in WT macrophages. Thus, expression of *olah* in macrophages increased lipid droplet formation following viral infection, leading to elevated cytokine production.

Since oleic acid, the major catalytic product of OLAH-mediated lipogenesis, is increased in patients hospitalized with respiratory infections (Figure 2C), we investigated its impact on infection *in vivo*. We infected WT mice fed on an oleic acid-enriched diet (WT$^{OA\ diet}$ mice) and age-matched WT mice fed on a normal diet, with a non-lethal X31 dose. In WT$^{OA\ diet}$ mice, we detected higher lung viral titers and greater body weight loss, particularly during early infection (days 2–5; Figure 7B), demonstrating that increased dietary intake of oleic acid leads to more severe influenza. We examined how oleic acid treatment of macrophages affected viral protein production and cytokine responses following infection. Oleic acid treatment of infected *olah*$^{-/-}$ and WT macrophages increased NP$^+$ and M$^+$ cell frequencies compared with untreated macrophages ($p < 0.001$ for both NP and M) (Figures 7C and S6D). Frequencies of viral protein-expressing cells in oleic acid-treated WT macrophages were higher than treated *olah*$^{-/-}$ macrophages (NP: $p < 0.001$; M: $p = 0.036$), presumably due to the presence of endogenous oleic acid.

Although oleic acid treatment increased cytokine production by uninfected WT and *olah*$^{-/-}$ macrophages (compared with untreated controls; *olah*$^{-/-}$: $p = 0.016$; WT: $p = 0.006$), exposure of these cells to infection further increased cytokine responses (both $p < 0.001$) and again with higher levels in WT compared with *olah*$^{-/-}$ macrophages ($p = 0.005$; Figure 7D). In *olah*$^{-/-}$ macrophages, differences between infected and uninfected cells were not evident without oleic acid and only observed between infected and uninfected WT macrophages ($p = 0.010$). However, the addition of oleic acid to *olah*$^{-/-}$ macrophages overcame this indifference to heighten not only virus-induced inflammatory responses but also antigen production.

As oleic acid can inhibit anti-viral action of IFITMs,[37] we investigated the impact of oleic acid treatment on influenza-infected macrophages from *ifitm3*$^{-/-}$ mice. Compared to influenza-infected WT macrophages, infection of *ifitm3*$^{-/-}$ macrophages increased infection (8 h $p \leq 0.001$; 24 h, $p \leq 0.003$; Figure 7E).[38] Frequency of infected macrophages between 8 and 24 h was similar, indicating that intracellular NP peaks early at 8 h post-infection. However, while oleic acid treatment of WT macrophages increased viral protein expression (8 h, $p = 0.014$; 24 h, $p < 0.001$), no significant effects were observed in *ifitm3*$^{-/-}$ macrophages, implicating that inhibition of IFITM3 by oleic acid may contribute to OLAH-mediated infection in these cells.

Influenza virus infection in WT was inhibited by fatty acid synthase inhibitors, 5-(tetradecyloxy)-2-furoic acid (TOFA) and C75[39,40] (TOFA, $p = 0.002$; C75, $p < 0.001$, Figure 7F), and to a lesser extent, reduced infection in *olah*$^{-/-}$ macrophages observed only using C75 ($p < 0.0461$), comparing to macrophages infected without inhibitors. However, culturing macrophages in the presence of the lipid droplet inhibitors, beauveriolide-I and ML-262,[41,42] decreased virus infection only in WT (beauveriolide-I, $p = 0.002$; ML-262, $p = 0.018$) but not *olah*$^{-/-}$ macrophages, in line with already diminished usage of lipid droplets in *olah*$^{-/-}$ macrophages. Altogether, while fatty acid synthesis supports influenza virus infection in WT macrophages, OLAH-mediated influenza virus infection outcomes depend on lipid droplet usage.

DISCUSSION

Although respiratory viral infections cause profound disease, underlying mechanisms are unclear, especially why some individuals present with mild infections while others succumb to respiratory disease.[5] When avian A(H7N9) emerged in humans with mortality of ~35%, we revealed that elevated inflammatory cytokines/chemokines early in infection predicted fatal H7N9 outcomes. Here, we investigated mechanisms associated with hypercytokinemia and fatal influenza disease. We identified *OLAH* as an early driver of severe A(H7N9) disease, seasonal influenza, COVID-19, RSV, and MIS-C. We demonstrated that influenza virus infection in *olah*$^{-/-}$ mice protected from lethal disease, stemming from reduced lung viral titers, tissue damage, pulmonary hypercytokinemia, innate cell infiltration, and lipid droplet formation, associated with differential lipid droplet dynamics, reduced viral infection, and inflammation in macrophages. Oleic acid, the main product of OLAH, exacerbated influenza infection and inflammatory potential of macrophages. Oleic acid also systemically increased in patients hospitalized with moderate-to-severe COVID-19. Elevated *OLAH* levels

Figure 5. *Olah* promotes influenza-induced lipid droplet formation and viral infection in the lungs

(A) Intracellular NP in CD64$^+$CD11b$^+$ macrophages and CD31$^-$EpCAM$^+$ epithelial cells from lungs of mice at day 1 after LD_{50} infection with X31 (n = 8/group).

(B) Contribution of immune and non-immune cells in driving OLAH-mediated disease severity. Bone marrow chimeras were established by adoptive transfer of donor bone marrow cells from WT or *olah*$^{-/-}$ mice into irradiated recipient mice (n = 10/group).

(C) After 8 weeks, mice were infected with a severe dose of X31; survival rates and body weights (mean ± SEM) monitored.

(D) Numbers of donor-derived WT (CD45.1$^+$) or *olah*$^{-/-}$ (CD45.2$^+$) macrophages and neutrophils (mean ± SEM) in lungs of LD_{50}-infected *olah*$^{-/-}$ (CD45.2$^+$) or WT (CD45.1$^+$) recipients, respectively, at day 1 post-infection.

(E) Lungs from mice following severe X31-infection (n = 3/group) were sliced (14 μm), fixed, and permeabilized prior to staining with antibodies to CD36 and influenza-NP, BODIPY for lipid droplets, and visualization by confocal microscopy. Representative single and merged (incorporating DAPI nuclei staining) images (×4 resolution) at each time point. Scale bars, 200 μm.

(F) Quantitation of lipid droplets from >150 cells in each image (at ×63 resolution) was performed from ≥9 different fields of view across the coverslip. LOESS regression lines with 95% confidence interval (CI) are shown.

(G) Viral titers (mean ± SD) in lungs following severe X31 infection (n = 5–9/group). Statistical analysis was performed by (A, C, right, and D) Mann-Whitney tests, (F and G) two-way ANOVA with Holms-Sidak post hoc test, and (C, left) Kaplan-Meier method.

See also Figures S4 and S7.

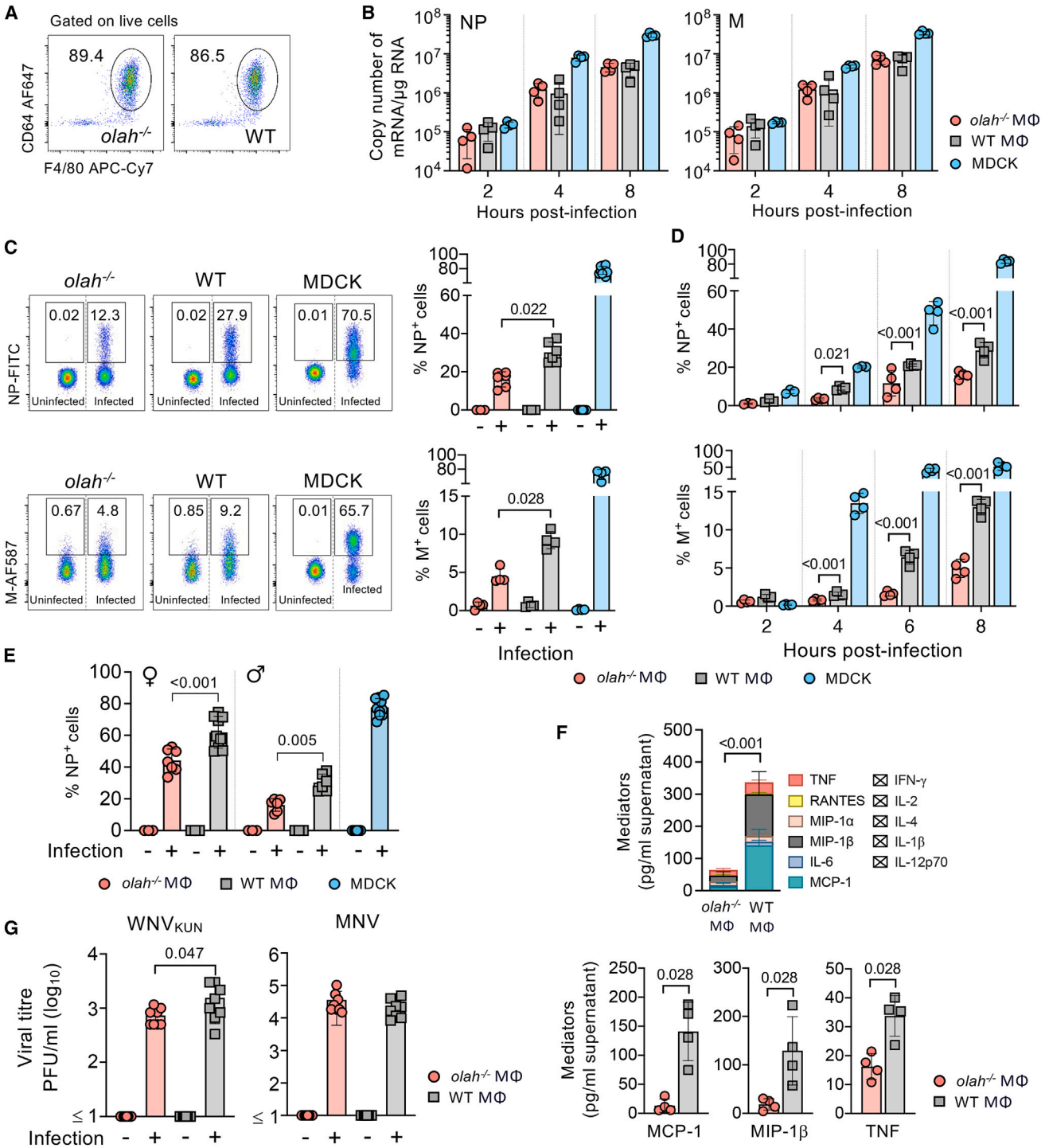

Figure 6. Increased viral protein expression and cytokine production in macrophages are driven by *olah* expression

(A) Co-expression of CD64 and F4/80 on peritoneal macrophages isolated from WT and *olah*$^{-/-}$ mice.

(B) Pooled macrophages or MDCK cells (n = 4/group) were infected with MOI = 4 X31. qPCR was performed for viral RNA encoding for NP or M (mean ± SD).

(C) Intracellular expression of viral protein in infected/uninfected macrophages and MDCK cells at 8 h post-infection (n = 4–5/group). Representative concatenated dot plots depicting frequencies of NP- or M-expressing F/480^{+} macrophages and MDCK cells from infected/uninfected cultures, with bar graphs showing mean ± SD within each group.

(D) Frequencies of intracellular NP- and M-expressing cells (mean ± SD) over 8 h post-infection (n = 4/group/time point).

(E) Segregation of NP-expressing macrophages into male or female mice (mean ± SD).

(legend continued on next page)

were previously reported in children experiencing neurological symptoms and pneumonia during H1N1pdm2009 infection.[43] These findings provide mechanistic insights into how elevated OLAH drives immunopathology and severe disease outcomes following respiratory infections.

OLAH-mediated inflammatory responses and severe disease outcomes were attributed to elevated cellular levels of fatty acids produced. Our observations agree with reports showing that viral infection can be exacerbated by oleic or palmitic acids.[16,37,44,45] Clinical reports of increased oleic acid levels and other catalytic products of OLAH in serum correlate with COVID-19 disease severity, RSV-induced asthma exacerbations, and acute respiratory distress syndrome (ARDS).[46–49] We demonstrate that exuberant pro-inflammatory cytokine responses observed during OLAH-mediated disease are associated with effects observed in influenza-infected macrophages. We found that *olah* expression did not affect susceptibility of macrophages to infection as viral mRNA remained unimpacted, suggesting that mechanisms facilitating virion attachment and internalization are not impacted by fatty acid availability. Viral protein levels were significantly reduced in *olah*$^{-/-}$ macrophages, indicating OLAH's role in promoting viral infection, suggesting a block in viral mRNA translation and/or in processes further upstream. As palmitoylation is a common modification of influenza virus glycoproteins and membrane proteins,[50] reduced amounts of fatty acids might affect the stability of viral proteins produced and their trafficking/degradation.[51]

Neutrophils and NK cells were also detected at higher levels in infected WT compared with *olah*$^{-/-}$ mice and might potentially contribute to OLAH-mediated disease. How OLAH is involved in recruitment of immune populations can be gleaned from oleic acid-induced lung injury animal models to study ARDS, where cell infiltration in response to tissue damage and inflammation are prominent hallmarks.[52,53] Our findings suggest a role for OLAH during infection of lung epithelial cells. Studies highlighted importance of palmitolylation of IFITMs for their anti-viral activity[54,55] and direct action of oleic acid in altering endosomal membrane fluidity and overcoming the ability of IFITMs to block HA-mediated fusion.[37] We observed negligible effects of oleic acid treatment on infectivity of *ifitm3*$^{-/-}$ macrophages; thus, any OLAH-mediated impact on IFITM3 activity in influenza-virus-infected cells might enhance early stages of viral infection at entry,[56] leading to enhanced viral production.

Given the function of OLAH in fatty acid biosynthesis, *olah* increases LDs in lungs and macrophages following infection, akin to cells infected with flaviviruses,[57,58] hepatitis C virus,[59] herpes simplex virus-1,[17] influenza.[17,60] Influenza-infected macrophages in WT mice were reduced by inhibiting lipid droplet formation, indicating that disease outcomes may depend on lipid droplet formation. Regarded as cellular energy sources to fuel viral life cycle events, these organelles are key in early anti-viral responses by mediating cytokine production.[17,35] Changes in fatty acids, including oleic and palmitic acids, impact macrophage functionality by direct signaling and/or reprogramming metabolic processes involved in cellular activation and polarization.[61,62] Lacking OLAH can establish a cellular state primed for viral control and regulated cytokine responses.

We defined the role of OLAH in driving severe influenza disease, underpinning impacts of fatty acids on immune dysfunction and viral infection. Having well-known host factors defining patients at risk of dying at hospital admission and the ability to predict the severity of disease early during respiratory viral infection is critical for alleviating disease and preventing deaths. Elevated *OLAH* expression could serve as a biomarker to predict disease outcome and inform how to manage/prioritize early interventions, including artificial ventilation or steroid administration, more effectively in patients at risk of dying. Our study proposes that OLAH could constitute a target for development of novel therapeutics to protect against severe respiratory diseases, including pandemic, avian/seasonal influenza, SARS-CoV-2, RSV, and MIS-C.

Limitations of the study

Although we found no associations between *olah* expression and BMI, age, or sex in COVID-19 patients, this cohort was young (0–21 years). While we provide mechanistic insights into how macrophages drive OLAH-mediated disease, involvement of other cells remains unknown. Due to lack of OLAH-specific antibodies, we could not determine OLAH protein levels. Future studies should explore how *OLAH* levels in humans are regulated and mechanisms of upregulation during infections. OLAH could play a role in exacerbation of non-respiratory infections. Analyses of virus-induced lipid droplet compositions may inform on how OLAH-mediated products regulate cytokine responses.

STAR★METHODS

Detailed methods are provided in the online version of this paper and include the following:

- KEY RESOURCES TABLE
- RESOURCE AVAILABILITY
  - Lead contact
  - Materials availability
  - Data and code availability
- EXPERIMENTAL MODEL AND STUDY PARTICIPANT DETAILS
  - Human study participants
  - Experimental mice
- METHOD DETAILS
  - Microarray-based transcriptomic analysis
  - Single-cell gene expression
  - RNA sequencing
  - Influenza virus infection of PBMCs
  - Quantitative polymerase chain reaction (qPCR)
  - Cytometric bead array

(F) Cytokine levels (mean ± SD) in supernatants of macrophages at 24 h post-infection (top). Crossed-out boxes indicate cytokines not detected. Depicted are individual cytokines (mean ± SD).
(G) West Nile Virus Kunjin (WNV_{KUN}) and murine norovirus (MNV) titers (mean ± SD) in supernatants of macrophages infected at MOI = 1 or MOI = 4, respectively, harvested at 24 h post-infection.
Statistical analysis was performed by (B and D) two-way ANOVA with Holms-Sidak post hoc test, (C, E, and F) Mann-Whitney test, and (G) Student's t test. See also Figure S6.

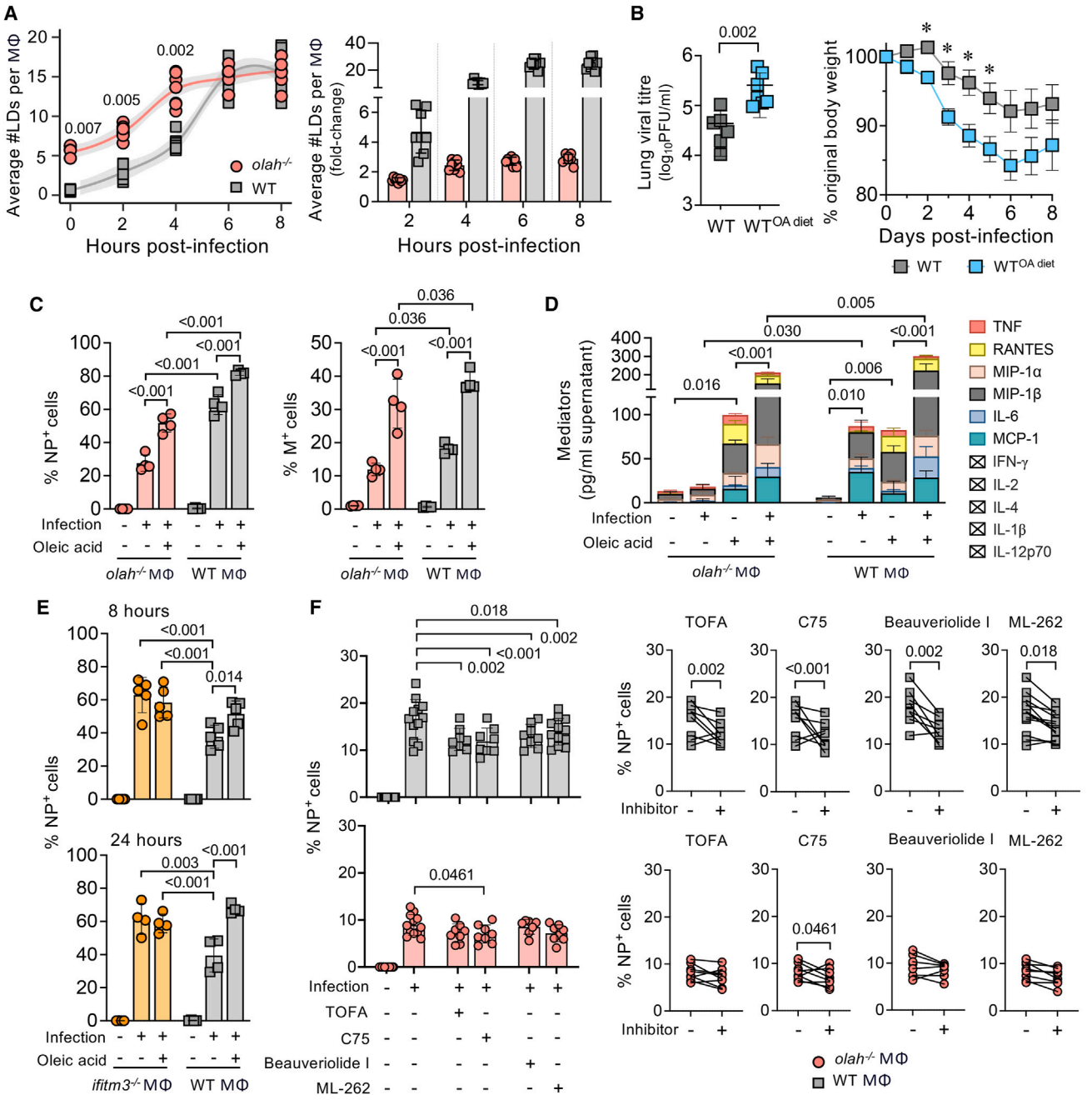

Figure 7. OLAH-mediated infection in macrophages is driven by oleic acid and lipid droplet usage

(A) Lipid droplets in influenza-infected macrophages were measured by infecting cells in chamber slides followed by BODIPY staining and visualization by confocal microscopy. Quantitation of lipid droplets was performed from >150 cells per image (×63 resolution) from 4 different fields of view/coverslip. LOESS regression line with 95% CI across time is shown. Fold-change in lipid droplet numbers post-infection was calculated relative to average numbers prior to infection.

(B) Male mice fed on an oleic acid rich diet ($WT^{OA\ diet}$) or normal chow (WT) were infected with X31 (10^4 PFU; n = 6/group) and monitored for body weight loss; lung viral titers (mean ± SD) measured at 5 days post-infection.

(C) Viral protein expression in macrophages (n = 4/group) cultured with 500 μM oleic acid prior and during infection. Frequencies of intracellular NP- or M-expressing cells (mean ± SD).

(D) Cytokine levels in supernatants (mean ± SD) at 24 h post-infection.

(E) Frequencies of intracellular NP-expressing WT and *ifitm3*$^{-/-}$ macrophages (n = 4–5/group) at 8 and 24 h post-infection following culture with oleic acid prior and during infection.

(legend continued on next page)

- Influenza virus infection of mice
- Bone marrow chimeras
- Determination of viral titres
- Intracellular protein and lipid droplets
- Tetramer and antibody staining
- Stimulation of T cells
- Infection of murine peritoneal macrophages
- Monophasic lipid extraction from mouse lungs
- Tandem mass spectrometry (MS/MS) analysis
- Lipidomics analysis of mouse lungs
- Proteomic sample preparation
- Data independent acquisition (DIA) analysis
- Human plasma preparation and lipidomics

● QUANTIFICATION AND STATISTICAL ANALYSIS

SUPPLEMENTAL INFORMATION

Supplemental information can be found online at https://doi.org/10.1016/j.cell.2024.07.026.

ACKNOWLEDGMENTS

Research was funded by the National Health and Medical Research Council of Australia: NHMRC-L1 to K.K. (#1173871), NHMRC-EL1 to T.H.O.N. (#1194036), and NHMRC Ideas Grant to B.Y.C. (#2001346). For purposes of open access, the authors have applied a CC BY public copyright license to any Author Accepted Manuscript version arising from this submission. We thank Weisan Chen for nucleoprotein reagents; Michael Inouye for assistance with analysis; Marumi Ohno for expertise in LD inhibitors; Drs. Loudovaris, Mannering, and Godfrey for spleen/thymus samples; and Richard Berger, Jinchun Sun, Gustavo Palacios, Armondo Flores-Torres, Lindsay Brown, and Shawn Campagna for lipidomic data assistance. We acknowledge the UoM Cytometry Platform, the UoM Mass Spectrometry/Bio21 Proteomics Facility Molecular Science and Biotechnology Institute, Latrobe Bioimaging Facility, St. Jude Children's Research Hospital Hartwell Center, Australian Phenomics Network Histopathology, the Organ Pathology Service, and the UoM Slide Scanning Service. *olah*$^{-/-}$ mice generation was supported by Phenomics Australia/Australian Government through National Collaborative Research Infrastructure Strategy. Reagents were obtained through NIH Biodefense and Emerging Infections Research Resources Repository, NIAID/NIH: Polyclonal Anti-Influenza Virus H3-Hemagglutinin, A/Hong Kong/1/68 (antiserum/Goat), and NR-3118. X.J. received a China Council-UoM Scholarship. J.C.C. and P.G.T. were supported by NIH NIAID R01-AI136514, U01AI150747, and ALSAC at St. Jude. R.C.M. is supported by a Ruth Kirschstein National Research Service Award Individual Postdoctoral Fellowship (#F32AI157296). A.G.R. and P.G.T. are supported by NIH NIAID R01-AI154470, C.E.v.d.S. by ARC-DECRA (#DE220100185), and N.E.S. by an ARC-Future Fellowship (#FT200100270). This project was funded with federal funds from the National Institute of Allergy and Infectious Diseases, the National Institutes of Health, the Department of Health and Human Services, contract #75N93021C00018 (NIAID Centers of Excellence for Influenza Research and Response, CEIRR) to K.K., P.G.T., and A.G.R. and contract #75N93021C00016 to H.S.S. We thank Overcoming COVID-19 Investigators for pediatric COVID-19 samples, supported by the US Centers for Disease Control and Prevention (individuals and enrolling sites: Adrienne Randolph, Janet Chou, Tanya Novak, Suden Kucukak, and Takuma Kobayashi, Boston Children's Hospital, Massachusetts; Michele Kong, Children's of Alabama, Birmingham; Mary Gaspers and Katri Typpo, Banner Children's Hospital, Tucson, Arizona; Katherine Irby and Ronald Sanders, Jr., Arkansas Children's Hospital, Little Rock; Natalie Cvijanovich, UCSF Benioff Children's Hospital, Oakland, California; Matt Zinter, UCSF Benioff Children's Hospital, California; Aline Maddux, Children's Hospital Colorado, Aurora; Brandon Chatani, Holtz Children's Hospital, Miami, Florida; Keiko Tarquinio, Children's Healthcare of Atlanta at Egleston, Atlanta; Bria Coates, Ann & Robert Lurie Children's Hospital, Chicago, Illinois; Courtney M. Rowan, MSCR, Riley Children's Hospital, Indianapolis, Indiana; Heidi Flori and Mary Dahmer, University of Michigan CS Mott Children's Hospital, Ann Arbor; Janet Hume, University of Minnesota Masonic Children's Hospital, Minneapolis; Emily Levy, Mayo Clinic, Rochester, Minnesota; Charlotte V. Hobbs, University of Mississippi Medical Center, Jackson; Jennifer Schuster, Children's Mercy Hospital, Kansas City; Melissa Cullimore, Children's Hospital & Medical Center, Omaha, Nebraska; Shira Gertz, Cooperman Barnabas Medical Center, Livingston, New Jersey; Stephanie Schwartz and Tracie Walker, University of North Carolina, Chapel Hill, North Carolina; Ryan Nofziger, Akron Children's Hospital, Ohio; Mary Allen Staat, Cincinnati Children's Hospital, Ohio; Steven Shein, University Hospitals Rainbow Babies and Children's Hospital, Cleveland, Ohio; Julie Fitzgerald, Children's Hospital of Philadelphia, Pennsylvania; Elizabeth Mack, MUSC Shawn Jenkins Children's Hospital, Charleston, South Carolina; Natasha Halasa, Monroe Carell Jr. Children's Hospital, Vanderbilt, Nashville, Tennessee; Laura Loftis, Texas Children's Hospital, Houston, Texas; and Hillary Crandall, Primary Children's Hospital, Salt Lake City, Utah). We thank CIViC-19 Investigators for adult COVID-19 plasma samples and Nicholas Hysmith; Chloe Hundman; Kristin McNair, RN; and Laura Boywid, RN, for clinical data. Some images were created with BioRender.com.

AUTHOR CONTRIBUTIONS

K.K. led the study. K.K., B.Y.C., Z.W., and J.C.C. supervised the study. K.K., B.Y.C., Z.W., X.J., K.J.H., S.L.L., E.A.M., J.C.C., R.C.M., T.F., A.M.G., L.L., H.S.S., P.G.T., and J.X. designed experiments. B.Y.C., X.J., J.C.C., D.G., R.C.M., L.-A.V.d.V., D.F.B., T.F., E.A.M., Y.W., Y.R., M.C., A.B., S.F., M.G.L., I.J.F., A.M.T., J.C.M., T.H.O.N., L.K., T.C., C.Y.W., L.H., A.C., M.A., D.L., J.R., and J.G.L. performed experiments. K.K., B.Y.C., X.J., Z.W., J.C.C., E.A.M., R.C.M., T.N., H.A.M., S.N., M.G.L., T.H.O.N., T.C., D.G., D.F.B., J.R.H., J.C.M., J.M.M., D.R.L., J.R., S.B., A.G.R., P.C.R., R.D.B., H.S.S., R.S.T., C.C., N.E.S., and P.G.T. analyzed data. K.K., E.A.M., K.J.H., A.K., M.J.H., S.F., C.E.v.d.S., S.L.L., N.E.S., S.N., and L.M.W. provided reagents. H.-F.K., L.M.W., X.J., S.P.B., K.L.F., and I.E.K. provided samples. K.K., B.Y.C., J.C.C., and X.J. wrote the manuscript. All authors reviewed/approved the manuscript.

DECLARATION OF INTERESTS

H.A.M. and B.Y.C. consult for Ena Respiratory. A.G.R. received research support from Illumina. P.G.T. is on the SAB of Immunoscape and Cytoagents, consulted for JNJ, received travel support/honoraria from Illumina and 10× Genomics, and has patents related to TCR discovery. J.C.C. and P.G.T. have patents related to treating or reducing severity of viral infections, including SARS-CoV-2.

Received: July 7, 2023
Revised: March 7, 2024
Accepted: July 17, 2024
Published: August 12, 2024

REFERENCES

1. WHO (2020). The top 10 causes of death. https://www.who.int/news-room/fact-sheets/detail/the-top-10-causes-of-death.
2. Krammer, F., Smith, G.J.D., Fouchier, R.A.M., Peiris, M., Kedzierska, K., Doherty, P.C., Palese, P., Shaw, M.L., Treanor, J., Webster, R.G., and Garcia-Sastre, A. (2018). Influenza. Nat. Rev. Dis. Primers *4*, 3.

(F) Intracellular NP in influenza-infected macrophages in presence or absence of TOFA (10 μg/mL), C75 (10 μg/mL), beauveriolide-I (10 μM), or ML-262 (1 μM) at 24 h post-infection.
Statistical analysis performed by (A and C–E) two-way ANOVA with Holms-Sidak post hoc test, (B) Mann-Whitney test, and (F) paired one-way ANOVA with Holms-Sidak post hoc test comparing treated and untreated macrophages derived from same mice. *$p < 0.05$.
See also Figure S4.

3. Short, K.R., Kedzierska, K., and van de Sandt, C.E. (2018). Back to the Future: Lessons Learned From the 1918 Influenza Pandemic. Front. Cell. Infect. Microbiol. *8*, 343.
4. Kalil, A.C., and Thomas, P.G. (2019). Influenza virus-related critical illness: pathophysiology and epidemiology. Crit. Care *23*, 258.
5. Puig-Barberà, J., Mira-Iglesias, A., Burtseva, E., Cowling, B.J., Serhat, U., Ruiz-Palacios, G.M., Launay, O., Kyncl, J., Koul, P., Siqueira, M.M., et al. (2019). Influenza epidemiology and influenza vaccine effectiveness during the 2015–2016 season: results from the Global Influenza Hospital Surveillance Network. BMC Infect. Dis. *19*, 415.
6. Dunning, J., Blankley, S., Hoang, L.T., Cox, M., Graham, C.M., James, P.L., Bloom, C.I., Chaussabel, D., Banchereau, J., Brett, S.J., et al. (2018). Progression of whole-blood transcriptional signatures from interferon-induced to neutrophil-associated patterns in severe influenza. Nat. Immunol. *19*, 625–635.
7. Mettelman, R.C., Souquette, A., Van de Velde, L.A., Vegesana, K., Allen, E.K., Kackos, C.M., Trifkovic, S., DeBeauchamp, J., Wilson, T.L., St. James, D.G., et al. (2023). Baseline innate and T cell populations are correlates of protection against symptomatic influenza virus infection independent of serology. Nat. Immunol. *24*, 1511–1526.
8. Nguyen, T.H.O., Koutsakos, M., van de Sandt, C.E., Crawford, J.C., Loh, L., Sant, S., Grzelak, L., Allen, E.K., Brahm, T., Clemens, E.B., et al. (2021). Immune cellular networks underlying recovery from influenza virus infection in acute hospitalized patients. Nat. Commun. *12*, 2691.
9. Oshansky, C.M., Gartland, A.J., Wong, S.S., Jeevan, T., Wang, D., Roddam, P.L., Caniza, M.A., Hertz, T., Devincenzo, J.P., Webby, R.J., and Thomas, P.G. (2014). Mucosal immune responses predict clinical outcomes during influenza infection independently of age and viral load. Am. J. Respir. Crit. Care Med. *189*, 449–462.
10. Everitt, A.R., Clare, S., Pertel, T., John, S.P., Wash, R.S., Smith, S.E., Chin, C.R., Feeley, E.M., Sims, J.S., Adams, D.J., et al. (2012). IFITM3 restricts the morbidity and mortality associated with influenza. Nature *484*, 519–523.
11. Wang, Z., Zhang, A., Wan, Y., Liu, X., Qiu, C., Xi, X., Ren, Y., Wang, J., Dong, Y., Bao, M., et al. (2014). Early hypercytokinemia is associated with interferon-induced transmembrane protein-3 dysfunction and predictive of fatal H7N9 infection. Proc. Natl. Acad. Sci. USA *111*, 769–774.
12. Allen, E.K., Randolph, A.G., Bhangale, T., Dogra, P., Ohlson, M., Oshansky, C.M., Zamora, A.E., Shannon, J.P., Finkelstein, D., Dressen, A., et al. (2017). SNP-mediated disruption of CTCF binding at the IFITM3 promoter is associated with risk of severe influenza in humans. Nat. Med. *23*, 975–983.
13. Lim, H.K., Huang, S.X.L., Chen, J., Kerner, G., Gilliaux, O., Bastard, P., Dobbs, K., Hernandez, N., Goudin, N., Hasek, M.L., et al. (2019). Severe influenza pneumonitis in children with inherited TLR3 deficiency. J. Exp. Med. *216*, 2038–2056.
14. Ciancanelli, M.J., Huang, S.X.L., Luthra, P., Garner, H., Itan, Y., Volpi, S., Lafaille, F.G., Trouillet, C., Schmolke, M., Albrecht, R.A., et al. (2015). Life-threatening influenza and impaired interferon amplification in human IRF7 deficiency. Science *348*, 448–453.
15. Hernandez, N., Melki, I., Jing, H., Habib, T., Huang, S.S.Y., Danielson, J., Kula, T., Drutman, S., Belkaya, S., Rattina, V., et al. (2018). Life-threatening influenza pneumonitis in a child with inherited IRF9 deficiency. J. Exp. Med. *215*, 2567–2585.
16. Limsuwat, N., Boonarkart, C., Phakaratsakul, S., Suptawiwat, O., and Auewarakul, P. (2020). Influence of cellular lipid content on influenza A virus replication. Arch. Virol. *165*, 1151–1161.
17. Monson, E.A., Crosse, K.M., Duan, M., Chen, W., O'Shea, R.D., Wakim, L.M., Carr, J.M., Whelan, D.R., and Helbig, K.J. (2021). Intracellular lipid droplet accumulation occurs early following viral infection and is required for an efficient interferon response. Nat. Commun. *12*, 4303.
18. Morita, M., Kuba, K., Ichikawa, A., Nakayama, M., Katahira, J., Iwamoto, R., Watanebe, T., Sakabe, S., Daidoji, T., Nakamura, S., et al. (2013). The lipid mediator protectin D1 inhibits influenza virus replication and improves severe influenza. Cell *153*, 112–125.
19. Tam, V.C., Quehenberger, O., Oshansky, C.M., Suen, R., Armando, A.M., Treuting, P.M., Thomas, P.G., Dennis, E.A., and Aderem, A. (2013). Lipidomic profiling of influenza infection identifies mediators that induce and resolve inflammation. Cell *154*, 213–227.
20. Wang, Z., Wan, Y., Qiu, C., Quiñones-Parra, S., Zhu, Z., Loh, L., Tian, D., Ren, Y., Hu, Y., Zhang, X., et al. (2015). Recovery from severe H7N9 disease is associated with diverse response mechanisms dominated by $CD8^+$ T cells. Nat. Commun. *6*, 6833.
21. Wang, Z., Zhu, L., Nguyen, T.H.O., Wan, Y., Sant, S., Quiñones-Parra, S.M., Crawford, J.C., Eltahla, A.A., Rizzetto, S., Bull, R.A., et al. (2018). Clonally diverse $CD38^+$ $HLA\text{-}DR^+CD8^+$ T cells persist during fatal H7N9 disease. Nat. Commun. *9*, 824.
22. Ritchie, M.K., Johnson, L.C., Clodfelter, J.E., Pemble, C.W., IV, Fulp, B.E., Furdui, C.M., Kridel, S.J., and Lowther, W.T. (2016). Crystal Structure and Substrate Specificity of Human Thioesterase 2: INSIGHTS INTO THE MOLECULAR BASIS FOR THE MODULATION OF FATTY ACID SYNTHASE. J. Biol. Chem. *291*, 3520–3530.
23. Salas, J.J., and Ohlrogge, J.B. (2002). Characterization of substrate specificity of plant FatA and FatB acyl-ACP thioesterases. Arch. Biochem. Biophys. *403*, 25–34.
24. Gao, R., Cao, B., Hu, Y., Feng, Z., Wang, D., Hu, W., Chen, J., Jie, Z., Qiu, H., Xu, K., et al. (2013). Human infection with a novel avian-origin influenza A (H7N9) virus. N. Engl. J. Med. *368*, 1888–1897.
25. Li, Q., Zhou, L., Zhou, M., Chen, Z., Li, F., Wu, H., Xiang, N., Chen, E., Tang, F., Wang, D., et al. (2014). Epidemiology of human infections with avian influenza A(H7N9) virus in China. N. Engl. J. Med. *370*, 520–532.
26. Mudd, P.A., Crawford, J.C., Turner, J.S., Souquette, A., Reynolds, D., Bender, D., Bosanquet, J.P., Anand, N.J., Striker, D.A., Martin, R.S., et al. (2020). Distinct inflammatory profiles distinguish COVID-19 from influenza with limited contributions from cytokine storm. Sci. Adv. *6*, eabe3024.
27. Feldstein, L.R., Tenforde, M.W., Friedman, K.G., Newhams, M., Rose, E.B., Dapul, H., Soma, V.L., Maddux, A.B., Mourani, P.M., Bowens, C., et al. (2021). Characteristics and Outcomes of US Children and Adolescents With Multisystem Inflammatory Syndrome in Children (MIS-C) Compared With Severe Acute COVID-19. JAMA *325*, 1074–1087.
28. Flerlage, T., Crawford, J.C., Allen, E.K., Severns, D., Tan, S., Surman, S., Ridout, G., Novak, T., Randolph, A., West, A.N., and Thomas, P.G. (2023). Single cell transcriptomics identifies distinct profiles in pediatric acute respiratory distress syndrome. Nat. Commun. *14*, 3870.
29. Liu, T.Y., Burke, T., Park, L.P., Woods, C.W., Zaas, A.K., Ginsburg, G.S., and Hero, A.O. (2016). An individualized predictor of health and disease using paired reference and target samples. BMC Bioinformatics *17*, 47.
30. Habibi, M.S., Thwaites, R.S., Chang, M., Jozwik, A., Paras, A., Kirsebom, F., Varese, A., Owen, A., Cuthbertson, L., James, P., et al. (2020). Neutrophilic inflammation in the respiratory mucosa predisposes to RSV infection. Science *370*, eaba9301.
31. Oemer, G., Koch, J., Wohlfarter, Y., Alam, M.T., Lackner, K., Sailer, S., Neumann, L., Lindner, H.H., Watschinger, K., Haltmeier, M., et al. (2020). Phospholipid Acyl Chain Diversity Controls the Tissue-Specific Assembly of Mitochondrial Cardiolipins. Cell Rep. *30*, 4281–4291.e4.
32. Ting, H.C., Chen, L.T., Chen, J.Y., Huang, Y.L., Xin, R.C., Chan, J.F., and Hsu, Y.-H.H. (2019). Double bonds of unsaturated fatty acids differentially regulate mitochondrial cardiolipin remodeling. Lipids Health Dis. *18*, 53.
33. Mallevaey, T., Clarke, A.J., Scott-Browne, J.P., Young, M.H., Roisman, L.C., Pellicci, D.G., Patel, O., Vivian, J.P., Matsuda, J.L., McCluskey, J., et al. (2011). A molecular basis for NKT cell recognition of CD1d-self-antigen. Immunity *34*, 315–326.
34. Hufford, M.M., Richardson, G., Zhou, H., Manicassamy, B., García-Sastre, A., Enelow, R.I., and Braciale, T.J. (2012). Influenza-infected neutrophils

within the infected lungs act as antigen presenting cells for anti-viral CD8+ T cells. PLoS One *7*, e46581.

35. Monson, E.A., Crosse, K.M., Das, M., and Helbig, K.J. (2018). Lipid droplet density alters the early innate immune response to viral infection. PLoS One *13*, e0190597.
36. Londrigan, S.L., Short, K.R., Ma, J., Gillespie, L., Rockman, S.P., Brooks, A.G., and Reading, P.C. (2015). Infection of Mouse Macrophages by Seasonal Influenza Viruses Can Be Restricted at the Level of Virus Entry and at a Late Stage in the Virus Life Cycle. J. Virol. *89*, 12319–12329.
37. Li, K., Markosyan, R.M., Zheng, Y.M., Golfetto, O., Bungart, B., Li, M., Ding, S., He, Y., Liang, C., Lee, J.C., et al. (2013). IFITM proteins restrict viral membrane hemifusion. PLoS Pathog. *9*, e1003124.
38. Londrigan, S.L., Wakim, L.M., Smith, J., Haverkate, A.J., Brooks, A.G., and Reading, P.C. (2020). IFITM3 and type I interferons are important for the control of influenza A virus replication in murine macrophages. Virology *540*, 17–22.
39. Landree, L.E., Hanlon, A.L., Strong, D.W., Rumbaugh, G., Miller, I.M., Thupari, J.N., Connolly, E.C., Huganir, R.L., Richardson, C., Witters, L.A., et al. (2004). C75, a fatty acid synthase inhibitor, modulates AMP-activated protein kinase to alter neuronal energy metabolism. J. Biol. Chem. *279*, 3817–3827.
40. Wang, C., Xu, C., Sun, M., Luo, D., Liao, D.F., and Cao, D. (2009). Acetyl-CoA carboxylase-alpha inhibitor TOFA induces human cancer cell apoptosis. Biochem. Biophys. Res. Commun. *385*, 302–306.
41. Namatame, I., Tomoda, H., Si, S., Yamaguchi, Y., Masuma, R., and Omura, S. (1999). Beauveriolides, specific inhibitors of lipid droplet formation in mouse macrophages, produced by Beauveria sp. FO-6979. J. Antibiot. (Tokyo) *52*, 1–6.
42. Zou, J., Ganji, S., Pass, I., Ardecky, R., Peddibhotla, M., Loribelle, M., Heynen-Genel, S., Sauer, M., Pass, I., Vasile, S., et al. (2010). Potent inhibitors of lipid droplet formation. In Probe Reports from the NIH Molecular Libraries Program (National Center for Biotechnology Information).
43. Yamashita, N., Tsukahara, H., Tsuge, M., Nagaoka, Y., Yashiro, M., Saito, Y., Fujii, Y., Oka, T., and Morishima, T. (2013). Pathogenic mechanisms of influenza A(H1N1)pdm09 infection elucidated on gene expression profiling. Pediatr. Int. *55*, 572–577.
44. Raini, S.K., Takamatsu, Y., Dumre, S.P., Urata, S., Mizukami, S., Moi, M.L., Hayasaka, D., Inoue, S., Morita, K., and Ngwe Tun, M.M. (2021). The novel therapeutic target and inhibitory effects of PF-429242 against Zika virus infection. Antiviral Res. *192*, 105121.
45. Ramphan, S., Suksathan, S., Wikan, N., Ounjai, P., Boonthaworn, K., Rimthong, P., Kanjanapruthipong, T., Worawichawong, S., Jongkaewwattana, A., Wongsiriroj, N., and Smith, D.R. (2017). Oleic acid Enhances Dengue Virus But Not Dengue Virus-Like Particle Production from Mammalian Cells. Mol. Biotechnol. *59*, 385–393.
46. Barberis, E., Timo, S., Amede, E., Vanella, V.V., Puricelli, C., Cappellano, G., Raineri, D., Cittone, M.G., Rizzi, E., Pedrinelli, A.R., et al. (2020). Large-Scale Plasma Analysis Revealed New Mechanisms and Molecules Associated with the Host Response to SARS-CoV-2. Int. J. Mol. Sci. *21*, 8623.
47. Shi, D., Yan, R., Lv, L., Jiang, H., Lu, Y., Sheng, J., Xie, J., Wu, W., Xia, J., Xu, K., et al. (2021). The serum metabolome of COVID-19 patients is distinctive and predictive. Metabolism *118*, 154739.
48. Dai, P., Tang, Z., Qi, M., Liu, D., Bajinka, O., and Tan, Y. (2022). Dispersion and utilization of lipid droplets mediates respiratory syncytial virus-induced airway hyperresponsiveness. Pediatr. Allergy Immunol. *33*, e13651.
49. Bursten, S.L., Federighi, D.A., Parsons, P., Harris, W.E., Abraham, E., Moore, E.E., Jr., Moore, F.A., Bianco, J.A., Singer, J.W., and Repine, J.E. (1996). An increase in serum C18 unsaturated free fatty acids as a predictor of the development of acute respiratory distress syndrome. Crit. Care Med. *24*, 1129–1136.
50. Wagner, R., Herwig, A., Azzouz, N., and Klenk, H.D. (2005). Acylation-mediated membrane anchoring of avian influenza virus hemagglutinin is essential for fusion pore formation and virus infectivity. J. Virol. *79*, 6449–6458.
51. Li, X., Shen, L., Xu, Z., Liu, W., Li, A., and Xu, J. (2022). Protein Palmitoylation Modification During Viral Infection and Detection Methods of Palmitoylated Proteins. Front. Cell. Infect. Microbiol. *12*, 821596.
52. Hussain, N., Wu, F., Zhu, L., Thrall, R.S., and Kresch, M.J. (1998). Neutrophil apoptosis during the development and resolution of oleic acid-induced acute lung injury in the rat. Am. J. Respir. Cell Mol. Biol. *19*, 867–874.
53. Mishra, P., Pandey, R., Pandey, N., Tripathi, S., and Tripathi, Y.B. (2022). Prevention of mortality in acute lung injury induced by oleic acid: Application of polyherbal decoction (bronco T). Front. Cell Dev. Biol. *10*, 1003767.
54. Das, T., Yang, X., Lee, H., Garst, E.H., Valencia, E., Chandran, K., Im, W., and Hang, H.C. (2022). S-Palmitoylation and Sterol Interactions Mediate Antiviral Specificity of IFITMs. ACS Chem. Biol. *17*, 2109–2120.
55. Klein, S., Golani, G., Lolicato, F., Lahr, C., Beyer, D., Herrmann, A., Wachsmuth-Melm, M., Reddmann, N., Brecht, R., Hosseinzadeh, M., et al. (2023). IFITM3 blocks influenza virus entry by sorting lipids and stabilizing hemifusion. Cell Host Microbe *31*, 616–633.e20.
56. Meischel, T., Fritzlar, S., Villalon-Letelier, F., Tessema, M.B., Brooks, A.G., Reading, P.C., and Londrigan, S.L. (2021). IFITM Proteins That Restrict the Early Stages of Respiratory Virus Infection Do Not Influence Late-Stage Replication. J. Virol. *95*, e0083721.
57. Barletta, A.B.F., Alves, L.R., Silva, M.C.L.N., Sim, S., Dimopoulos, G., Liechocki, S., Maya-Monteiro, C.M., and Sorgine, M.H.F. (2016). Emerging role of lipid droplets in Aedes aegypti immune response against bacteria and dengue virus. Sci. Rep. *6*, 19928.
58. Samsa, M.M., Mondotte, J.A., Iglesias, N.G., Assunção-Miranda, I., Barbosa-Lima, G., Da Poian, A.T., Bozza, P.T., and Gamarnik, A.V. (2009). Dengue virus capsid protein usurps lipid droplets for viral particle formation. PLoS Pathog. *5*, e1000632.
59. Bang, B.R., Li, M., Tsai, K.N., Aoyagi, H., Lee, S.A., Machida, K., Aizaki, H., Jung, J.U., Ou, J.J., and Saito, T. (2019). Regulation of Hepatitis C Virus Infection by Cellular Retinoic Acid Binding Proteins through the Modulation of Lipid Droplet Abundance. J. Virol. *93*, e02302-18.
60. Episcopio, D., Aminov, S., Benjamin, S., Germain, G., Datan, E., Landazuri, J., Lockshin, R.A., and Zakeri, Z. (2019). Atorvastatin restricts the ability of influenza virus to generate lipid droplets and severely suppresses the replication of the virus. FASEB J. *33*, 9516–9525.
61. Korbecki, J., and Bajdak-Rusinek, K. (2019). The effect of palmitic acid on inflammatory response in macrophages: an overview of molecular mechanisms. Inflamm. Res. *68*, 915–932.
62. Wu, H., Han, Y., Rodriguez Sillke, Y., Deng, H., Siddiqui, S., Treese, C., Schmidt, F., Friedrich, M., Keye, J., Wan, J., et al. (2019). Lipid droplet-dependent fatty acid metabolism controls the immune suppressive phenotype of tumor-associated macrophages. EMBO Mol. Med. *11*, e10698.
63. Boyd, D.F., Allen, E.K., Randolph, A.G., Guo, X.J., Weng, Y., Sanders, C.J., Bajracharya, R., Lee, N.K., Guy, C.S., Vogel, P., et al. (2020). Exuberant fibroblast activity compromises lung function via ADAMTS4. Nature *587*, 466–471.
64. Perez-Riverol, Y., Bai, J., Bandla, C., García-Seisdedos, D., Hewapathirana, S., Kamatchinathan, S., Kundu, D.J., Prakash, A., Frericks-Zipper, A., Eisenacher, M., et al. (2022). The PRIDE database resources in 2022: a hub for mass spectrometry-based proteomics evidences. Nucleic Acids Res. *50*, D543–D552.
65. Irizarry, R.A., Bolstad, B.M., Collin, F., Cope, L.M., Hobbs, B., and Speed, T.P. (2003). Summaries of Affymetrix GeneChip probe level data. Nucleic Acids Res. *31*, e15.

66. Smyth, G.K. (2004). Linear models and empirical bayes methods for assessing differential expression in microarray experiments. Stat. Appl. Genet. Mol. Biol. *3*, Article3.

67. Stuart, T., Butler, A., Hoffman, P., Hafemeister, C., Papalexi, E., Mauck, W.M., III, Hao, Y., Stoeckius, M., Smibert, P., and Satija, R. (2019). Comprehensive Integration of Single-Cell Data. Cell *177*, 1888–1902.e21.

68. Martin, M. (2011). Cutadapt removes adapter sequences from high-throughput sequencing reads. EMBnet. J. *17*, 3.

69. Dobin, A., Davis, C.A., Schlesinger, F., Drenkow, J., Zaleski, C., Jha, S., Batut, P., Chaisson, M., and Gingeras, T.R. (2013). STAR: ultrafast universal RNA-seq aligner. Bioinformatics *29*, 15–21.

70. Li, B., and Dewey, C.N. (2011). RSEM: accurate transcript quantification from RNA-Seq data with or without a reference genome. BMC Bioinformatics *12*, 323.

71. Robinson, M.D., McCarthy, D.J., and Smyth, G.K. (2010). edgeR: a Bioconductor package for differential expression analysis of digital gene expression data. Bioinformatics *26*, 139–140.

72. Ritchie, M.E., Phipson, B., Wu, D., Hu, Y., Law, C.W., Shi, W., and Smyth, G.K. (2015). limma powers differential expression analyses for RNA-sequencing and microarray studies. Nucleic Acids Res. *43*, e47.

73. Law, C.W., Alhamdoosh, M., Su, S., Dong, X., Tian, L., Smyth, G.K., and Ritchie, M.E. (2016). RNA-seq analysis is easy as 1-2-3 with limma, Glimma and edgeR. F1000Res *5*, 1408.

74. Bachem, A., Makhlouf, C., Binger, K.J., de Souza, D.P., Tull, D., Hochheiser, K., Whitney, P.G., Fernandez-Ruiz, D., Dahling, S., and Kastenmuller, W. (2019). Microbiota-Derived Short-Chain Fatty Acids Promote the Memory Potential of Antigen-Activated $CD8^+$ T Cells. Immunity *51*, 285–297.e5.

75. Deliyannis, G., Wong, C.Y., McQuilten, H.A., Bachem, A., Clarke, M., Jia, X., Horrocks, K., Zeng, W., Girkin, J., Scott, N.E., et al. (2021). TLR2-mediated activation of innate responses in the upper airways confers antiviral protection of the lungs. JCI Insight *6*, e140267.

76. Hyde, J.L., Sosnovtsev, S.V., Green, K.Y., Wobus, C., Virgin, H.W., and Mackenzie, J.M. (2009). Mouse norovirus replication is associated with virus-induced vesicle clusters originating from membranes derived from the secretory pathway. J. Virol. *83*, 9709–9719.

77. Mikulasova, A., Gillespie, L.K., Ambrose, R.L., Aktepe, T.E., Trenerry, A.M., Liebscher, S., and Mackenzie, J.M. (2021). A Putative Lipid-Associating Motif in the West Nile Virus NS4A Protein Is Required for Efficient Virus Replication. Front. Cell Dev. Biol. *9*, 655606.

78. Lydic, T.A., Townsend, S., Adda, C.G., Collins, C., Mathivanan, S., and Reid, G.E. (2015). Rapid and comprehensive 'shotgun' lipidome profiling of colorectal cancer cell derived exosomes. Methods *87*, 83–95.

79. Liebisch, G., Fahy, E., Aoki, J., Dennis, E.A., Durand, T., Ejsing, C.S., Fedorova, M., Feussner, I., Griffiths, W.J., Köfeler, H., et al. (2020). Update on LIPID MAPS classification, nomenclature, and shorthand notation for MS-derived lipid structures. J. Lipid Res. *61*, 1539–1555.

80. Hughes, C.S., Foehr, S., Garfield, D.A., Furlong, E.E., Steinmetz, L.M., and Krijgsveld, J. (2014). Ultrasensitive proteome analysis using paramagnetic bead technology. Mol. Syst. Biol. *10*, 757.

81. Hughes, C.S., Moggridge, S., Müller, T., Sorensen, P.H., Morin, G.B., and Krijgsveld, J. (2019). Single-pot, solid-phase-enhanced sample preparation for proteomics experiments. Nat. Protoc. *14*, 68–85.

82. Harney, D.J., Hutchison, A.T., Hatchwell, L., Humphrey, S.J., James, D.E., Hocking, S., Heilbronn, L.K., and Larance, M. (2019). Proteomic Analysis of Human Plasma during Intermittent Fasting. J. Proteome Res. *18*, 2228–2240.

83. Kulak, N.A., Pichler, G., Paron, I., Nagaraj, N., and Mann, M. (2014). Minimal, encapsulated proteomic-sample processing applied to copy-number estimation in eukaryotic cells. Nat. Methods *11*, 319–324.

84. Rappsilber, J., Mann, M., and Ishihama, Y. (2007). Protocol for micro-purification, enrichment, pre-fractionation and storage of peptides for proteomics using StageTips. Nat. Protoc. *2*, 1896–1906.

85. Tyanova, S., Temu, T., Sinitcyn, P., Carlson, A., Hein, M.Y., Geiger, T., Mann, M., and Cox, J. (2016). The Perseus computational platform for comprehensive analysis of (prote)omics data. Nat. Methods *13*, 731–740.

86. Cao, Z., Schmitt, T.C., Varma, V., Sloper, D., Beger, R.D., and Sun, J. (2020). Evaluation of the Performance of Lipidyzer Platform and Its Application in the Lipidomics Analysis in Mouse Heart and Liver. J. Proteome Res. *19*, 2742–2749.

STAR★METHODS

KEY RESOURCES TABLE

REAGENT or RESOURCE	SOURCE	IDENTIFIER
Antibodies		
CD3 eBio500A2 AF700	Invitrogen	Cat#56003382; RRID:AB_837094
CD3 145-2C11 PerCP-Cy5.5	BD Biosciences	Cat#551163; RRID AB_394082:
CD8 53-6.7 AF700	Biolegend	Cat#100730; RRID: AB_493703
CD8 53-6.7 PE	Biolegend	Cat#100708; RRID: AB_312747
CD8 53-6.7 PerCP-Cy5.5	BD Biosciences	Cat#551162; RRID: AB_394081
CD4 GK1.5 APC-Cy7	BD Biosciences	Cat#552051; RRID: AB_394331
CD38 90 PE-Cy7	Biolegend	Cat#102718; RRID: AB_2275531
I-Ab AF6-120.1 Pacific Blue	Biolegend	Cat#116422; RRID: AB_10613473
CD44 IM7 FITC	BD Biosciences	Cat#553133; RRID: AB_2076224
CD44 IM7 AF700	BD Biosciences	Cat#560567; RRID: AB_1727480
CD44 IM7 APC-Cy7	Biolegend	Cat#103028; RRID: AB_830785
CD62L MEL-14 BV570	Biolegend	Cat#104433; RRID: AB_10900262
CD62L MEL-14 PE-Cy7	Biolegend	Cat#104418; RRID: AB_313103
CD45.1 A20 APC-Cy7	Biolegend	Cat#110716; RRID: AB_313505
CD45.1 A20 FITC	BD Pharmingen	Cat#553775; RRID: AB_10926208
CD45.2 104 BV711	BD Biosciences	Cat#563685; RRID: AB_2738374
CD45.2 104 BV786	BD Horizon	Cat#563686; RRID: AB_2738375
TCRva2 B20.1 PE-Cy7	BD Biosciences	Cat#560624; RRID: AB_1727584
CD11b M1/70 FITC	Invitrogen	Cat#11011282; RRID:AB_464935
CD11b M1/70 BV605	BD Biosciences	Cat#563015; RRID: AB_2737951
CD11c N418 FITC	Invitrogen	Cat#11011482; RRID: AB_464940
CD11c HL3 PE	BD Biosciences	Cat#553802; RRID: AB_395061
CD19 6D5 FITC	Biolegend	Cat#115506; RRID: AB_313641
NK1.1 PK136 FITC	Biolegend	Cat#108706; RRID: AB_313393
NK1.1 PK136 PE	BD Biosciences	Cat#553165; RRID: AB_394677
F4/80 BM8 FITC	Invitrogen	Cat#11480185; RRID: AB_2637191
F4/80 BM8 APC-Cy7	Biolegend	Cat#123118; RRID: AB_893477
Ly6G 1A8 PE-Cy7	BD Biosciences	Cat#560601; RRID: AB_1727562
CD64 X54-5/7.1 AF647	BD Biosciences	Cat#558539; RRID: AB_647120
CD64 139309 BV421	Biolegend	Cat#139309; RRID: AB_2562694
SiglecF E50-2440 PECF594	BD Biosciences	Cat#562757; RRID: AB_2687994
Ly6C AL-21 AF700	BD Biosciences	Cat#561237; RRID: AB_10612017
EpCam G8.8 APC-Cy7	Biolegend	Cat#118218; RRID: AB_2098648
CD31 390 BV421	Biolegend	Cat#102433; RRID: AB_2629682
CD45 30-F11 PerCP	BD Biosciences	Cat#557235; RRID: AB_396609
TCRgd GL3 BV421	BD Biosciences	Cat#562892; RRID: AB_2737871
TCRβ H57-597 BV711	BD Biosciences	Cat#563135; RRID: AB_2738023
CD27 LG.3A10 PerCP-Cy5.5	Biolegend	Cat#124214; RRID: AB_2275577
IFN-γ XMG1.2 FITC	Biolegend	Cat#505806; RRID: AB_315400
TNF-α MP6-XT22 APC	BD Biosciences	Cat#554420; RRID: AB_398553
IL-2 JES6-5H4 PE	BD Biosciences	Cat#554428; RRID: AB_395386
iNOS 6 FITC	BD Transduction Laboratories	Cat#610330; RRID: AB_397721
Arg-1 A1exF5 AF700	Invitrogen	Cat#56-3697-82; RRID: AB_2734833

(*Continued on next page*)

Continued

REAGENT or RESOURCE	SOURCE	IDENTIFIER
CD206 MR6F3 PE	Invitrogen	Cat#12-2061-82; RRID: AB_2637422
IAV-Nucleoprotein 1331 FITC	GeneTex	Cat# GTX36902; RRID:AB_11179672
IAV-Matrix GA2B	Bio-Rad	Cat# MCA401; RRID: AB_322157
IAV-H3 HA, A/Hong Kong/1/68	BEI Resources	Cat#BEI NR-3118; RRID: Unavailable
Anti-Goat Ig AF633	Invitrogen	Cat#A-21082; RRID: AB_2535739
Anti-Mouse-Ig AF568	Invitrogen	Cat# A-11031; RRID: AB_144696
Streptavidin – PE	BD Biosciences	Cat#554061; RRID: AB_10053328
Streptavidin – APC	BD Biosciences	Cat#554067; RRID: AB_10050396
Alexa Fluor 555	Life technologies	Cat#A-21422; RRID:AB_2535844
Biological samples		
Human peripheral blood samples from H7N9 influenza infected adult patients	Shanghai Public Health Clinical Center (SHAPHC). National Major R&D Program 92169206, National Natural Sciences Foundation of China (2014-E030 and 2014-E032)	N/A
Human peripheral blood samples from COVID-19 pediatric cohort	Overcoming COVID-19 Study at Boston Children's Hospital (IRB-P00033157)	N/A
Human peripheral blood samples from SARS-CoV-2 infected patients for lipidomic analysis	CIViC-19 study (IRB 20-07345-FB and IRB 20-0654)	N/A
Human peripheral blood samples from healthy individuals	Australian Red Cross Lifeblood (West Melbourne, Australia) (Ethics ID 2015#8)	N/A
Human tissue samples	Lung samples were from Alfred Hospital Lung tissue Biobank (Melbourne, Australia) (Ethics ID 13344). Thymus was obtained from Royal Children's Hospital (Melbourne, Australia) and Melbourne Children's Heart Tissue Bank (Ethics IDs 38192, 24131, and 24567), spleens were provided by DonateLife Victoria (Melbourne, Australia) (Ethics ID 13344), and tonsil samples were obtained from the Launceston General Hospital (Tasmania, Australia) (Ethics IDs H0017479 and 24567).	N/A
Chemicals, peptides, and recombinant proteins		
PAXgene Blood RNA Kit	QIAGEN	Cat#762164
PAXgene Blood RNA Tubes	QIAGEN	Cat#762165
Qubit HS RNA Assay Kit	ThermoFisher	Cat#Q32852
Golgi Plug	BD Biosciences	Cat#555029
RNeasy Mini Kit	QIAGEN	Cat#74106
OneStep RT-PCR Kit	QIAGEN	Cat#210212
OLAH-specific probes human: Hs00217864_m1,	Thermo Fisher	Cat#4331182
OLAH-specific probes mouse: Mm00521437_m1	Thermo Fisher	Cat#4331182
actin probe human: Hs01060665_g1	Thermo Fisher	Cat#4331182
actin probe mouse: Mm00607939_s1	Thermo Fisher	Cat#4331182
qPCR primers for influenza A NP gene: forward 5′ CCGGAACCCAGGAATG, reverse 5′ GAGTGCAAGACCGTGCTAGAA; qPCR primers for influenza A M gene: forward 5′ GACCRATCCTGTCAC CTCTGAC, reverse 5′ GGGCAT TYTGGACAAKC GTCTACG	Sigma	N/A
collagenase III	Worthington Biochemical Corporation	Cat#LS004182
DNase I	Sigma-Aldrich, Germany	Cat# 04536282001

(*Continued on next page*)

Continued

REAGENT or RESOURCE	SOURCE	IDENTIFIER
Leibovitz L15 medium	Gibco	Cat#41300-039
Trypsin	Worthington Biochemical, NJ, USA	Cat#LS003648
$NP_{366-374}$-peptide	Genescript	N/A
$PA_{224-233}$-peptide	Genescript	N/A
oleic acid	Sigma-Aldrich, Australia	Cat#SLCM9550
BODIPY 493/503	Life technologies	Cat#D3922
MitoTracker Deep Red FM	Invitrogen	Cat#M22426
2-NBDG	Invitrogen	Cat#N13195
Image-iT TMRM	Invitrogen	Cat#I34361
TOFA	Abcam	Cat#ab141578
C75	Sigma	Cat#C5490
Beauveriolide I	Cayman Chemical, USA	Cat#13-31774
ML-262	Cayman Chemical, USA	Cat#13-21902
DAPI	Sigma	Cat#D9542
Fixable Live/Dead Aqua Blue viability dye	Life Technologies	Cat#L34957
Cytofix/Cytoperm Plus kit	BD Biosciences	Cat#555028
eBioscience FOXP3 staining Buffer Set	Thermo Fisher	Cat#00-5523-00
Sodium dodecyl sulfate (SDS)	Sigma Aldrich Pty. Ltd.	Cat#L3771-500G; CAS#151-21-3
Tris(hydroxymethyl)methylamine	Thermo Fisher Scientific	Cat#A18494-36; CAS#77-86-1
Dithiothreitol	Bio-Rad Laboratories Pty. Ltd.	Cat#1610611; CAS#3483-12-3
Iodoacetamide	Sigma Aldrich Pty. Ltd.	Cat#I1149-5G; CAS#144-48-9
Ethyl alcohol, Pure 200 proof, HPLC/spectrophotometric grade	Sigma Aldrich Pty. Ltd.	Cat#459836-2L; CAS#64-17-5
Trypsin/Lys-c	Promega	Cat#V5073
2-propanol HPLC plus	Sigma Aldrich Pty. Ltd.	Cat#650447-2.5L; CAS#67-63-0
Trifluoroacetic acid (TFA)	Sigma Aldrich Pty. Ltd.	Cat#T6508-5ML; CAS#76-05-1
Methanol HPLC Gradient grade	Thermo Fisher Scientific	Cat#M/4058/17; CAS#67-56-1
Ethyl acetate hypergrade for LC-MS	Sigma Aldrich Pty. Ltd.	Cat#1036491000; CAS#141-78-6
Ammonium hydroxide (25%) for LC-MS	Sigma Aldrich Pty. Ltd.	Cat#5330030050; CAS#1336-21-6
Acetonitrile HPLC GRADIENT GRADE	Sigma Aldrich Pty. Ltd.	Cat#34851-4L; CAS#75-05-8
Dimethyl sulfoxide (DMSO) HPLC GRADIENT GRADE	Thermo Fisher Scientific	Cat#AA22914M1; CAS#67-68-5
Formic acid	Sigma Aldrich Pty. Ltd.	Cat#F0507-100ML; CAS#64-18-6
Deposited data		
Microarray data from patients infected with A(H7N9)	This paper	GEO: GSE268303
RNAseq data from COVID-19 cohort	This paper	BioProject: PRJNA1116218
scRNAseq of healthy lungs	Boyd et al.[63]	BioProject: PRJNA613670
scRNASeq of blood from ICU influenza patients	Mudd et al.[26]	BioProject: PRJNA630932; SRA: SRR11233662
scRNAseq of tracheal aspirates from patients with pARDS	Flerlage et al.[28]	BioProject: PRJNA971535
Microarray data from human viral challenge models	Liu et al.[29]	GEO: GSE73072
Bulk RNAseq data from nasal curettage cells obtained in a controlled human RSV infection trial	Habibi et al.[30]	GEO: GSE155237
Mass spectrometry proteomics data from mouse macrophages	This paper	PRIDE: PXD048155
Lipidomics data from mouse lung samples	This paper	NMDR: ST003290

(*Continued on next page*)

Continued

REAGENT or RESOURCE	SOURCE	IDENTIFIER
Software and algorithms		
R v3.03	https://www.r-project.org/	N/A
R v4.2.1	https://www.r-project.org/	N/A
QuantStudio 6 and 7 Pro Real-Time PCR Systems	Applied Biosystems	N/A
ZEISS 800 confocal microscope	Zeiss	N/A
ZEN blue edition software	Zeiss	N/A
ImageJ software	National Institutes of Health, USA	N/A
FlowJo v10.5.3	FlowJo LLC, Becton Dickinson	N/A
Prism v8.3.1 or v9.1.0	GraphPad	N/A
BD FACS Diva v8.0.1	BD Biosciences	N/A
BD Fortessa II or BD FACS Canto II	BD Biosciences	N/A
FCAP Array software	Soft Flow Inc., Hungary	N/A
MD Dial 4.9	CompMS	N/A
CellRanger v3.0.2	10x Genomics	N/A
Other		
Affymetrix GeneChip Human Gene 2.0 ST Array for transcriptomic analysis	Gene Tech (Shanghai)	N/A
Agilent High Sensitivity ScreenTape	Agilent	Cat#5067-5579
SPLASH LIPIDOMIX Mass Spec Standard	Avanti Polar Lipids, Birmingham, AL, USA	Cat#330707
Deuterated saturated/monounsaturated fatty acid standards	Cayman Chemical, USA	Cat#30654
Sera-Mag speedbeads Carboxylate (hydrophobic)	GE Healthcare Life Sciences	Cat#45152105050250
Sera-Mag speedbeads Carboxylate (hydrophilic)	GE Healthcare Life Sciences	Cat#65152105050250
Empore Polystyrene-divinylbenzene, reversed-phase sulfonate (SDB-RPS) Material	Sigma Aldrich Pty. Ltd.	Cat#66886-U
Pepmap100 C18 (20 mm × 75 μm) trap column	Thermo Fisher Scientific	THC164946
Pepmap C18 (500 mm × 75 μm) analytical column	Thermo Fisher Scientific	THC164570

RESOURCE AVAILABILITY

Lead contact

Further information and requests for resources and reagents should be directed to and will be fulfilled by the lead contact, Katherine Kedzierska (kkedz@unimelb.edu.au).

Materials availability

The *olah*$^{-/-}$ mice generated in this study are available from the lead contact upon request with a completed and approved Materials Transfer Agreement.

Data and code availability

- Microarray data from patients infected with A(H7N9) have been deposited in the Gene Expression Omnibus under accession GEO: GSE268303.
- Bulk RNAseq data from healthy participants, pediatric patients hospitalized with SARS-CoV-2 infection, and pediatric patients hospitalized with MIS-C have been deposited in the NCBI Sequence Read Archive (SRA) under BioProject: PRJNA1116218.
- This paper analyzes existing published gene expression datasets available under BioProject: PRJNA613670 (scRNAseq of healthy lungs), BioProject: PRJNA630932 and SRA: SRR11233662 (scRNAseq of blood from ICU influenza patients),

BioProject: PRJNA971535 (scRNAseq of tracheal aspirates from patients with pARDS), and GEO: GSE73072 (human respiratory virus challenge).

- Lipidomics data from lungs of naïve and infected mice have been deposited in National Metabolomics Data Repository (NMDR) under accession number NMDR: ST003290.
- Mass spectrometry proteomics data have been deposited to the ProteomeXchange Consortium under PRIDE[64]: PXD048155.
- Microscopy data reported in this paper will be shared by the lead contact upon request.
- This paper does not contain original code.
- Any additional information required to reanalyze the data reported in this paper is available from the lead contact upon request.

EXPERIMENTAL MODEL AND STUDY PARTICIPANT DETAILS

Human study participants

All information on sex, age and demographics of human participants, where available, were collected as indicated on patient records. Patients infected with A(H7N9) influenza virus were admitted to the Shanghai Public Health Clinical Center (SHAPHC) between March and August 2013 and their clinical details have been previously published.[20] The age and gender of these patients are listed in Table S1. For our study, longitudinal blood samples from 8 patients were analyzed; 4 who recovered (a73, a134, a20 and a9) and 4 who succumbed (a118, a33, a131 and a22). Informed consent was obtained from all participants and the study was approved and conducted under supervision by the SHAPHC Ethics Committee (National Major R&D Program 92169206) and under the ethics IDs 2014-E030 and 2014-E032. Peripheral blood was collected in heparinized tubes and peripheral blood monocular cells (PBMCs) were isolated via Ficoll-Paque separation. PBMCs were also isolated from buffy packs sourced from the Australian Red Cross Lifeblood (West Melbourne, Australia under the ethics ID 2015#8. Lung samples from deceased organ donors were obtained via the Alfred Hospital Lung Tissue Biobank (Melbourne, Australia) and spleens were provided by DonateLife Victoria (Melbourne, Australia) under The University of Melbourne ethics ID 13344. Thymus was obtained from Royal Children's Hospital (Melbourne, Australia) and Melbourne Children's Heart Tissue Bank (ethics ID 38192) and approved by the human research ethics committees of the Murdoch Children's Research Institute (ethics ID 24131) and The University of Melbourne (ethics ID 24567). The donor's guardians provided informed written consent prior to surgery. Tonsil samples were obtained from the Launceston General Hospital (Tasmania, Australia) under the Tasmanian Health and Medical ethics ID H0017479 and The University of Melbourne ethics ID 24567.

For the COVID-19 pediatric cohort, PAXgene whole blood samples were obtained from hospitalized COVID-19 pediatric patients, or patients with MIS-C, aged <21 years recruited across US pediatric hospitals as part of the Overcoming COVID-19 Study under a single IRB at Boston Children's Hospital (IRB-P00033157). The demographics of this cohort are listed in Table S2. Blood samples were collected early after admission. Patient disease severity was grouped according to degree of respiratory involvement comparing 43 children with no to minimal respiratory dysfunction and requiring no major respiratory support other than oxygen or nebulizers, to 25 with moderate to severe respiratory dysfunction requiring respiratory support with high flow nasal cannula oxygen or non-invasive ventilation, to 23 with life-threatening respiratory failure requiring invasive mechanical ventilation and some of these also required extracorporeal membrane oxygenation (1 died). Samples from 22 uninfected, healthy individuals recruited at St Jude Children's Research Hospital (Memphis, TN, USA) as part of the FLU09 cohort[9] were also used as controls in this study.

For the lipidomic analyses of participants who were ambulatory or hospitalized with SARS-CoV-2 infection, our study used plasma samples and data collected from the CIViC-19 study. CIViC-19 is an ongoing test-negative-case-control observational study approved by the Institutional Review Boards of The University of Tennessee Health Science Center (UTHSC) and St. Jude Children's Research Hospital in Memphis, TN (IRB numbers 20-07345-FB and 20-0654, respectively). Participants were recruited from Le Bonheur Children's Hospital, Methodist Germantown Hospital, Methodist University Hospital, and UTHSC's outpatient community COVID-19 testing sites. CIViC-19 study participants or their legal guardians provided written informed consent in compliance with 45 CFR46 and the Declaration of Helsinki regarding ethical principles for medical research. Non-English-speaking persons, pregnant women, and those who could not provide informed consent themselves or via a designated decision maker were excluded from this study. Individuals tested for SARS-CoV-2 due to symptoms or known exposure were included in the CIViC-19 study. Participants from the CIViC-19 cohort included in our study were considered COVID-19 positive if SARS-CoV-2 polymerase chain reaction (PCR) tests conducted in clinical laboratory was positive. Seventy-three SARS-CoV-2 PCR positive outpatient (n = 38) and hospitalized (n = 35) participants aged >16 years were included in our study (Table S4). Blood was collected from these participants immediately after enrolment on visit day 1. Briefly, blood was drawn into BD vacutainer CPT cell preparation tubes (BD Biosciences, Franklin Lakes, NJ, USA) with sodium citrate. Blood was processed the day of collection per manufacturer guidelines and plasma stored at −80°C.

For pARDS analysis, we leveraged existing data from tracheal aspirate samples obtained from RSV infected children aged 0-2 recruited at LeBonheur Children's Hospital (Memphis, TN, USA)[28] with 5 experiencing no to mild (n = 5) pediatric ARDS (pARDS), 7 with moderate to severe pARDS as well as 5 with non-RSV related infection but with moderate to severe pARDS and 6 control patients who were children without acute lower respiratory tract infection or lung injury.

Experimental mice

C57BL/6 mice were bred and maintained in the Biological Research Facility in the Department of Microbiology and Immunology at The University of Melbourne. Following weaning (~3 weeks old), mice were placed on a normal maintenance diet (Barastoc, Ridley Corporation, Australia). In some cases, mice were fed with a semi-pure high fat rodent diet containing 7.7% oleic acid (93.4% of total monounsaturated fat content) and 5.8% palmitic acid (57.8% of total saturated fat content) (Diet SF04-001, Specialty Feeds, Australia) for at least 12 weeks before use. All animal experimentation was conducted in accordance with the Australian National Health and Medical Research Council Code of Practice for the Care and Use of Animals for Scientific Purposes Guidelines and institutional regulations following approval (permit numbers 1714304, 1614073 and 20532) by The University of Melbourne Animal Ethics Committee. Both female and male mice 7–15 weeks of age were used for experiments.

An *olah*-deficient (*olah*$^{-/-}$) mouse strain on a C57BL/6 background was generated by constitutive knock out of the *olah* allele on chromosome 2 via CRISPR/Cas9-mediated gene editing. All embryonic procedures and generation of founder mice were performed at the Melbourne Advanced Genome Editing Center (Walter Eliza Hall Institute, Australia). Deletion of exons 1 and 2 of the *olah* allele using sgRNAs to target sites (with the sequence TGACAGCCATCTATACACGG and GCGAGATAAAGCCTACTGAC) flanking these exons resulted in the deletion of 4467bp. To detect the resulting sequence following deletion, forward (GGCTGCATTTCTCTCTTTA TGG) and reverse (GGGATGTGAGAAGGAAAAGG) primers were used to confirm the presence of a 312bp PCR product. Presence or absence of the wildtype allele was also performed using forward and reverse primer sequences, CTCAGACTCCGGTTCTGGAC and GAGGTCCCTTGTGTGTCTCC, respectively, to produce a product of 311bp. DNA samples from founder mice positive for the deleted allele were sequenced and confirmed by alignment to the predicted excised sequence prior to selection for breeding to produce homozygous knockouts. The genotyping of all breeding pairs and their first 2 generations of offspring was performed by Transnetyx (Tennessee, USA) using real-time PCR.

METHOD DETAILS

Microarray-based transcriptomic analysis

Peripheral blood (2 ml) was collected from each patient, preserved in PAXgene Blood RNA Tubes (QIAGEN) and stored at −80°C until use. Total RNA was extracted using a PAXgene Blood RNA Kit (QIAGEN) and transcriptomic analysis performed by Gene Tech (Shanghai) using a Affymetrix GeneChip Human Gene 2.0 ST Array. All analyses used the R statistical programming environment (v3.03). Raw CEL intensity files underwent 'Perfect Match' probe set-level normalization including background correction using robust multiarray averaging (RMA), quantile normalization and summarization of gene expression using the median published algorithm.[65] Probe set intensity distributions between arrays (before and after normalization) and MA plots of the log intensity ratio versus the average log intensity were assessed for excessive technical variability. The early phase sample from patient a20 was excluded from analysis as the interquartile range of the expression deviation was substantially outside that exhibited by all other samples. Unexpressed probe sets, exhibiting less fluorescence than background probes and w a PSDABG P value > 0.05 were removed from subsequent analyses. The LIMMA package was used to identify differentially expressed probe sets.[66] "Fatal" and "Recovered" cohorts were compared using an empirical Bayes procedure to moderate standard error, and a t test was used to test for difference in expression levels. Corresponding *p* values were adjusted for multiple testing using the Benjamini & Hochberg approach. Differentially expressed genes were defined by *p* value <0.05 and an absolute $\log_2$ fold-change of $\geq$2.0. For human challenge studies, microarray data were obtained from accession GEO: GSE73072, processed as described above, and *OLAH* expression was analysed using mixed effects models with the *lme4* package in R to test for effects of time and infection status, with subject coded as a random effect.

Single-cell gene expression

For previously published single-cell datasets, data were processed and analysed exactly as indicated in the corresponding manuscript, with new figures generated using Seurat.[67] For example, for healthy donor lung single-cell data, samples from a non-smoker were obtained from the NDRI, viable CD45$^+$ and CD45$^-$ fractions were sorted into distinct populations, processed using the 5′ gene expression kit following manufacturer instructions (10X Genomics), and sequenced on an Illumina HiSeq 2000.[63] Data from the CD45$^+$ and CD45$^-$ libraries were processed using CellRanger (v3.0.2; 10X Genomics) and aggregated with CellRanger aggr using default parameters, and downstream analyses were conducted in Seurat.[63]

RNA sequencing

Whole blood from consented participants was collected directly into PAXgene Blood RNA Tubes using standard phlebotomy practices and immediately stabilized for storage at −80°C. Total RNA was isolated from PAXgene whole blood collection tubes on a QIAcube Connect MDx system using the PAXgene Blood RNA Kit following the manufacturer's instructions. Briefly, PAXgene tube contents were thawed at RT for 2 h to ensure RBC lysis then centrifuged for 10 min at 4,000 xg to pellet, washed, and resuspended. The resulting nucleic acid-containing pellets were transferred into 2 mL processing tubes, treated with proteinase K, and placed into the QIAcube worktable. The QIAcube automated further sample processing through a PAXgene Shredder spin column ensuring homogenization, binding total RNA (>18 nt) to a PAXgene RNA spin column, treatment with DNase-I (15 min at 30°C) to eliminate genomic DNA (gDNA), and final elution. Purified RNA samples were denatured for 5 min at 65°C in preparation for

downstream applications. For FLU09 healthy control samples, total RNA was extracted from PBMCs by lysis and separation of aqueous phase using Trizol Reagent (Invitrogen) and the RNeasy Mini Kit (Qiagen) with DNase-I digestion. To ensure quality RNA sequencing, purified RNA samples were screened and selected for high total RNA integrity ($RIN^e \geq 7$) and low genomic DNA contamination using Agilent High Sensitivity ScreenTape run on a 2200 TapeStation. RNA concentration was determined by Qubit HS RNA Assay Kit and a minimum of 300 ng total RNA was submitted for RNA sequencing. Sequencing libraries were generated with the Illumina TruSeq Stranded Total RNA with Ribo-Zero Globin and rRNA depletion kit and sequenced at 100×100bp on an Illumina NovaSeq 6000.

Raw sequencing reads were trimmed using the Trim Galore wrapper for CutAdapt[68] with default parameters before alignment to the GRCh38 reference using STAR (v2.7.9a)[69] with GENCODE annotations (v31). RSEM (v1.3.1)[70] was used to quantify gene counts, and edgeR[71] and limma[72] were used for CPM calculation and normalization and modelling differential expression across severity groups while controlling for differences in days between symptom onset and sample collection, sex, whether a patient was previously healthy, steroid administration prior to sample collection, identification of a bacterial coinfection, age category, race, and ethnicity. *p* values were adjusted for multiple testing using the Benjamini & Hochberg FDR method. Glimma[73] was used for data exploration. For analysis of published bulk RNAseq from nasal curettage cells obtained after controlled human RSV infection, data were obtained from accession GEO: GSE155237 and analysed in the same manner but using annotated counts provided by the original study.[30]

Influenza virus infection of PBMCs

Thawed PBMCs (1.5×10^6) were infected with A/California/07/2009 (H1N1) at a MOI of 4 for 1 hour at 37°C and 5% CO_2 in RPMI-1640 media supplemented 2mM L-glutamine, 1mM MEM sodium pyruvate, 100μM MEM non-essential amino acids, 5mM HEPES buffer solution, 55μM 2-mercaptoethanol, 100 U/ml penicillin and 100 μg/ml streptomycin. Fetal calf serum was then added to achieve a 10% concentration (v/v) and incubated for a further 3 hours followed by the addition of Golgi Plug (BD Biosciences; final concentration of 1mg/ml). After 18 hours, cells were harvested and analysed for intracellular IAV nucleoprotein (NP) expression (Figure S7A).

Quantitative polymerase chain reaction (qPCR)

Tissues were collected in RNAlater (Thermo Fischer) or processed into single cell suspensions. RNA was extracted from tissue or cell samples using an RNeasy Mini Kit (QIAGEN). Gene expression levels were determined using a OneStep RT-PCR Kit (QIAGEN), with probes specific for genes encoding for OLAH (human: Hs00217864_m1, mouse: Mm00521437_m1, Thermo Fisher) and actin (human: Hs01060665_g1, mouse: Mm00607939_s1, Thermo Fisher). To detect influenza gene expression levels encoding for viral antigens, the following primers were used; forward primer 5′ CCGGAACCCAGGAATG; and reverse primer 5′ GAGTGCAAGACCGTG CTAGAA for NP, and forward primer 5′ GACCRATCCTGTCAC CTCTGAC; and reverse primer 5′ GGGCATTYTGGACAAKC GTCTACG for M. Standards for both NP and M were run alongside the tested samples to generate a standard and copy numbers per μg RNA were interpolated. qPCR was performed and analyzed on QuantStudio 6 and 7 Pro Real-Time PCR Systems (Applied Biosystems).

Cytometric bead array

Cytokines and chemokines in human plasma were previously quantified using the human inflammatory cytokine kit or a human soluble protein flex-set system (BD Biosciences) as previously reported.[11] Mouse tissue homogenates and macrophage culture supernatants were assayed using a murine soluble protein flex-set system (BD Biosciences) according to the manufacturer's instructions. All samples were analysed using a BD FACSAria II or BD FACS Canto II (BD Biosciences). Data were analysed using FCAP Array software (Soft Flow Inc., Hungary).

Influenza virus infection of mice

Influenza virus infection was performed under light anaesthesia with isofluorane and intranasal instillation (30μl) with 10^4 to 10^5 plaque forming units (PFU) of A/HK/x31 (X31; H3N2). Mice were culled when a humane endpoint was reached; ≥25% of original body weight lost. For lethal LD_{50}-infection, mice were infected with a viral titre that results in 50% mortality rate. All virus stocks were dose-titrated in mice to determine the LD_{50} dose prior to experimental use. An LD_{50} dose of 1×10^5 PFU was used for experiments in Figures 4B–4F and 5E–5G, and 2×10^4 PFU was used in Figures 4G, 4H, and 5A–5D. All harvested tissues were passed through 70 μm cell sieves to obtain single-cell suspensions. For the lungs, enzymatic digestion in collagenase III (Worthington Biochemical Corporation, USA; 1 mg/mL) and DNase I (Sigma-Aldrich, Germany; 0.5 mg/mL) for 30 min at 37°C was performed prior to this. Bronchoalveolar lavages were collected by flushing the lungs *in situ* with 1ml of PBS by means of a 23G needle inserted into the trachea and cells obtained by centrifugation. Where necessary, cell suspensions were incubated with 0.15 M NH_4Cl and 17 mM Tris-HCl at pH 7.2 for 5 min at 37°C to lyse red blood cells. To prepare samples for histopathology, whole tissues and organs were collected into PBS containing 10% formalin and sent for analysis at the Phenomics Australia Histopathology Slide Scanning Service (The University of Melbourne, Australia).

Bone marrow chimeras

Bone marrow chimeras were established using a method previously described.[74,75] Briefly, CD45.1-expressing C57BL/6 WT and *olah*$^{-/-}$ mice were lethally irradiated with 2 doses of 5.5 Gy 3 hours apart and reconstituted with 5×10^6 T cell-depleted bone marrow cells from CD45.2- or CD45.1-expressing WT or *olah*$^{-/-}$ mice. Donor and recipient cells were discriminated by isoform expression

(CD45.1 or CD45.2) *in vivo*. Mice were depleted of radioresistant T cells on the following day by i.p. injection with anti-Thy1 antibody (clone T24; in the form of 100μL of cell culture supernatant manufactured in-house). Animals were maintained on antibiotics (neomycin and polymyxin B, Millipore Sigma) contained in drinking water for 6 weeks. Chimeric mice were allowed to reconstitute for at least 8 weeks. Using flow cytometry staining with CD45.1 and CD45.2-specific antibodies, we have validated each of our chimeras has high reconstitution rates (>90%) of cells of the proper phenotype *in vivo* (Figure S4A).

Determination of viral titres

Clarified supernatants from centrifuged homogenized lungs of influenza-infected mice were assayed for titres of infectious virus in plaque assays using Madin Darby canine kidney (MDCK) cells cultured in six-well plates.[75] Briefly, supernatants were added to confluent MDCK layers and held for 1 hour at 37°C. Monolayers were then overlaid with Leibovitz L15 medium containing 0.9% agarose and 2μg/ml of Trypsin (Worthington Biochemical, NJ, USA). Plates were incubated at 37°C and 5% CO_2 for 3 days and virus-mediated cell lysis counted as plaques on the monolayer and expressed as plaque forming units (PFU).

Clarified supernatants from macrophage cultures *in vitro* infected with murine norovirus (MNV) were assayed for titres as previously described.[76] Briefly, supernatants were added to confluent monolayers of RAW264.7 cells and for 1 hour at 37°C. Cells were overlaid with 2 ml of medium containing 70% DMEM, 2.5% FCS, 15 mM $NaHC0_3$, 5 U of penicillin-streptomycin, 25 mM HEPES, 2 mM Glutamax, and 0.35% low-melting-point agarose/well and incubated at 37°C and 5% CO_2 for 2 days. Cells were fixed by adding 1 ml of 4% formaldehyde/well directly onto the overlay and held for 30 min at room temperature before rinsing with water and staining with 0.2% crystal violet for 20 min, to visualise and count plaques. Titres of West Nile Virus, Kunjin strain (WNV_{KUN}), was performed as previously described[77] where supernatants were added to confluent monolayers of VERO cells instead and held for 2 hours before overlay with 1ml of the same media as above, except 44% DMEM and 0.8% carboxymethylcellulose was used (instead of agarose), and incubated at 37°C and 5% CO_2 for 3 days before fixing and staining as above.

Intracellular protein and lipid droplets

Lungs were inflated with optimum cutting temperature fluid and snapped frozen prior to slicing into 14μm sections with a Leica CM 3050 S cryostat and mounting on microscope slides for storage at -80°C. For analysis, sections were fixed with 4% paraformaldehyde (Sigma) for 15 min at room temperature, permeabilised with 0.1% Triton X-100 (Sigma T9284-500ml) for 10 min and blocked with 1% BSA for 30 mins. Sections were stained with anti-IAV nucleoprotein (IAV-NP) (Prof Weisan Chen, La Trobe University) for 1 hour then washed and incubated with Alexa Fluor 555 (Life technologies) secondary antibody for 1 hour. BODIPY 493/503 (Life technologies) was used to stain for lipid droplets (LDs) at 1ng/ml for 1 hour at room temperature and nuclei were stained with DAPI (Sigma) for 5 min. Vectashield Antifade Mounting Medium (Vector Laboratories) was added prior to imaging on a ZEISS 800 confocal microscope. Droplet numbers were analysed from acquired z-stack maximum intensity projection images (Zeiss ZEN blue edition software) in ImageJ software (National Institutes of Health, USA) using the particle analysis tool and normalised to average LDs per cell. For each sample, at least 9 fields of view from different locations across the coverslip were imaged at 63× magnification. For enumeration of LDs in influenza-infected peritoneal macrophages (see below), cells were seeded into 8-well glass chamber slides (Nunc, USA) and fixed and permeabilised as indicated above. At least 4 fields of view for each replicate were imaged.

Tetramer and antibody staining

Cells were stained with Fixable Live/Dead AquaBlue viability dye (Life Technologies) at room temperature for 10 mins. For peptide MHC (pMHC) tetramer staining, cells were incubated $D^bNP_{366-374}$-APC and $D^bPA_{224-233}$-PE for 60 mins in FACS Buffer (PBS containing 0.5% BSA and 2mM EDTA) at room temperature in the dark. Surface antibody staining was performed in 50 μl FACs Buffer for 30 mins at 4°C. Various combinations of fluorochrome-conjugated antibodies were used (key resources table) with specific gating strategies to define distinct cell populations (Figures S7B–S7E). For intracellular antibody staining, cells were fixed and permeabilised following surface antibody staining using a Cytofix/Cytoperm Plus kit (BD Biosciences) as per the manufacturer's instructions unless specified below. Following washing with Perm Wash buffer (BD Biosciences), cells were stained with fluorochrome-conjugated antibodies in 50 μl of the same buffer for 30 mins at 4°C. To detect intracellular IAV-NP, cells were fixed and permeabilised using an eBioscience FOXP3 staining kit (Thermo Fisher) instead as per the manufacturer's instructions and stained using FITC-anti-IAV NP antibody (Sapphire Biosciences). For detection of intracellular M, cells were first fixed with 4% PFA for 30 mins, then permeabilized with 0.1%Triton X-100 for 15 mins at 4°C, followed by staining with anti-M antibody (Bio-Rad) and AF568-anti mouse Ig. To detect surface HA expression, cells were stained with polyclonal anti-H3 HA (A/Hong Kong/1/68) in the form of goat antiserum (BEI resources) and an AF633-anti-goat Ig (Invitrogen). All staining using metabolic markers Mitotracker-APC, 2-DNBG-FITC and TMRM-PE were performed at 37°C following surface staining with antibodies. Samples were acquired on a BD FACSAria II or BD LSR Fortessa flow cytometer and data was analyzed by Flowjo Software version 10 (FlowJo LLC, Becton, Dickinson).

Stimulation of T cells

To measure influenza-specific T cell responses in mice, cells from lungs, BAL and spleen were harvested at day 10 post-infection and seeded onto U-bottom 96-well plates (Sigma-Aldrich) and incubated at 37°C and 5% CO_2 for 5 hours in cRPMI (RPMI-1640 media supplemented with 2mM L-glutamine, 1mM MEM sodium pyruvate, 100μM MEM non-essential amino acids, 5mM HEPES buffer solution, 55μM 2-mercaptoethanol, 100 U/ml penicillin, 100 μg/ml streptomycin and 10% fetal calf serum [all Gibco]) containing

1mg/ml Golgi-Plug (BD Biosciences) and 10 U/ml recombinant human IL-2 (Roche Diagnostics, Basel, Switzerland) in the absence or presence of 1mM $NP_{366-374}$ or $PA_{224-233}$-peptide. Cells were subsequently stained for surface markers and intracellular cytokines and analysed by flow cytometry as described above.

Infection of murine peritoneal macrophages

Peritoneal cells were obtained by *in situ* lavage of the peritoneal cavity three times with 5ml of FACS Buffer. Exudate cells from WT or *olah*$^{-/-}$ mice were pooled, centrifuged and red blood cells lysed before seeding in 24-well plates (10^6 cells/ml) for 4 hours at 37°C and 5% CO_2 in cDMEM (DMEM media supplemented with 2mM L-glutamine, 1mM MEM sodium pyruvate, 100 U/ml penicillin, 100 μg/ml streptomycin and 10% fetal calf serum [all Gibco]). Following removal of non-adherent cells, 5ml of FACS Buffer was added for 5 min and adherent cells detached by gentle pipetting. Collected cells were then re-seeded in cDMEM at 2-5 x 10^5 cells/250 μl in a flat-bottom 96-well plate overnight and infected the following day with X31 influenza virus in serum-free DMEM at an MOI of 4 for 1 hour. Infections using WNV_{KUN} and MNV was performed at an MOI of 1 and 5, respectively, for 2 hours. Virus was then aspirated, and media replaced with fresh serum-free DMEM until harvest for analysis. For treatment of macrophages with fatty acid synthase or lipid droplet inhibitors, the replaced media was supplemented with TOFA (Abcam; 10 μg/ml), C75 (Sigma; 10 μg/ml), Beauveriolide I (Cayman Chemical; 10 μM) or ML262 (Cayman Chemical; 1 μM). For treatment of macrophages with oleic acid, exudate cells were cultured overnight in cDMEM supplemented with oleic acid (500 μM; Sigma-Aldrich, Australia) prior to infection the next day and maintained in fresh serum-free DMEM containing oleic acid until harvest for analysis.

Monophasic lipid extraction from mouse lungs

Whole lungs were harvested, weighed, minced and freeze dried. Prior to lipid extraction, freeze dried lungs were incubated with 200 μl of ice-cold 60% methanol containing 0.01% (w/v) butylated hydroxytoluene (BHT) and incubated overnight at −20°C. SPLASH LIPIDOMIX Mass Spec Standard (10μl; Cat. 330707, Avanti Polar Lipids, Birmingham, AL, USA) and deuterated saturated/monounsaturated fatty acid standards (10μl; Cayman Chemical, USA) were added to each sample and tissue homogenised with a Bullet Blender (Next Advance, Troy, NY, USA) and sonicated for 20 minutes. Monophasic lipid extraction was performed according to Lydic et al.[78] wherein 120 μl of water, 420 μl of methanol with 0.01% (w/v) BHT, and 270 μl of chloroform were added to all samples prior to thorough vortexing and incubated on a shaker at 1400 rpm for 30 mins. Following centrifugation, supernatants containing lipids were transferred to new tubes and the remaining pellets re-extracted by adding 100μl of water and 400μl of chloroform:methanol (1:2 v/v) containing 0.01% (w/v) BHT and incubation on a shaker at 1000 rpm for 15 mins. Supernatants from each extraction round were pooled, dried by evaporation under vacuum and freeze-dried. Lyophilised samples were then resuspended in chloroform:methanol (1:9 v/v) containing 0.01% BHT and centrifuged to remove precipitates.

Tandem mass spectrometry (MS/MS) analysis

Samples were analyzed by ultrahigh performance liquid chromatography (UHPLC) coupled to tandem mass spectrometry (MS/MS) employing a Vanquish UHPLC linked to an Orbitrap Fusion Lumos mass spectrometer (Thermo Fisher Scientific, San Jose, CA, USA), with separate runs in positive and negative ion polarities. Solvent A was 6/4 (v/v) acetonitrile/water with 5 mM medronic acid and solvent B was 9/1 (v/v) isopropanol/acetonitrile. Both solvents A and B contained 10 mM ammonium acetate. 10 uL of each sample was injected into an Acquity UPLC HSS T3 C18 column (1 x 150 mm, 1.8 μm; Waters, Milford, MA, USA) at 50°C at a flow rate of 60 μl/min for 3 min using 3% solvent B. During separation, the percentage of solvent B was increased from 3% to 70% in 5 min and from 70% to 99% in 16 min. Subsequently, the percentage of solvent B was maintained at 99% for 3 min. Finally, the percentage of solvent B was decreased to 3% in 0.1 min and maintained for 3.9 min. All MS analysis were performed using an electrospray ionization source (3.5 kV in positive- and 3.0 kV in negative ionization-mode). In both polarities, the flow rates of sheath, auxiliary and sweep gases were 25 and 5 and 0 arbitrary unit(s), respectively. The ion transfer tube and vaporizer temperatures were maintained at 300°C and 150°C, respectively, and the ion funnel RF level was set at 50%. From 3 to 24 min, top speed data-dependent scan with a cycle time of 1 s was used. Within each cycle, a full-scan MS-spectra were acquired firstly in the Orbitrap at a mass resolving power of 120,000 (at m/z 200) across an m/z range of 300–2,000 using quadrupole isolation, an automatic gain control (AGC) target of 4^5 and a maximum injection time of 50 milliseconds, followed by higher-energy collisional dissociation (HCD)-MS/MS at a mass resolving power of 15,000 (at m/z 200), a normalized collision energy (NCE) of 27% at positive mode and 30% at negative mode, an m/z isolation window of 1, a maximum injection time of 35 milliseconds and an AGC target of 5e4. For the improved structural characterization of glycerophosphocholine (PC) lipid cations, a data-dependent product ion (m/z 184.0733)-triggered collision-induced dissociation (CID)-MS/MS scan was performed in the cycle using a q-value of 0.25 and a NCE of 30%, with other settings being the same as that for HCD-MS/MS. For the improved structural characterization of triacylglycerol (TG) lipid cations, the fatty acid + NH3 neutral loss product ions observed by HCD-MS/MS were used to trigger the acquisition of the top-3 data-dependent ion trap CID-MS^3 scans in the cycle using a q-value of 0.25 and a NCE of 30%, with other settings being the same as that for HCD-MS/MS. Dynamic exclusion of 15 seconds was enabled and only ions with charge state of 1-3 were selected for fragmentation.

Lipidomics analysis of mouse lungs

LC-MS/MS data was searched through MS Dial 4.90. The mass accuracy settings are 0.005 Da and 0.025 Da for MS1 and MS2. The minimum peak height is 50000 and mass slice width is 0.05 Da. The identification score cut off is 80%. Post identification was done

with a text file containing name and m/z of each standard. In positive mode, [M+H]+, [M+NH4]+ and [M+H-H2O]+ were selected as ion forms. In negative mode, [M−H]− and [M+CH3COO]− were selected as ion forms. All lipid classes available were selected for the search. PC, LPC, DG, TG, CE, SM were identified and quantified at positive mode while FA, PE, LPE, PS, LPS, PG, LPG, PI, LPI, PA, LPA, Cer, CL were identified and quantified at negative mode. The retention time tolerance for alignment is 0.1 min. Lipids with maximum intensity less than 5-fold of average intensity in blank were removed. All other settings were default. All lipid LC-MS features were manually inspected and re-integrated when needed. These four types of lipids; 1) lipids with only sum composition except SM and PC, 2) lipid identification due to peak tailing, 3) retention time outliner within each lipid class, 4) LPA and PA artifacts generated by in-source fragmentation of LPS and PS were also removed. The shorthand notation used for lipid classification and structural representation follows the nomenclature proposed previously.[79] Quantification of lipid species in the unit of pmol/100 mg of lung tissue from each sample was achieved by normalizing the LC peak areas of identified lipids against those of the corresponding internal lipid standards in the same lipid class, the quantity of each lipid standard at pmol, and finally the weight of lung tissue. For the lipid classes without correspondent stable isotope-labelled lipid standards, the LC peak areas of individual molecular species within these classes were normalized as follows: the MG species against the DG (18:1D7_15:0); the LPG against the PG(18:1D7_15:0), the LPA against the PA(18:1D7_15:0), the LPS against the PS (18:1D7_15:0), and the Cer against the SM(d18:1_18:1D9). LipidSigR (version 0.99.0) R package was used to log transform normalised lipid concentrations prior to comparison by multiple t-test (package rstatix version 0.7.2) with p values < 0.01 considered significant. Volcano plots and heatmaps were generated using EnhancedVolcano (version 1.14.0) and ComplexHeatmap (version 2.12.1) respectively.

Proteomic sample preparation

Isolated macrophages were lysed in 4% SDS, 100 mM Tris pH 8.5 by boiling at 90°C for 10 minutes with shaking at 2000 rpm before being prepared using the SP3 sample preparation approach.[80,81] Samples were reduced with Dithiothreitol (20 mM) for 10 minutes at 90°C and alkylated with Iodoacetamide (40 mM) for 40 minutes at room temperature in the dark. 500 μg of Milli-Q water prewashed Sera-mag speed magnetic beads (GE Healthcare) were added to samples and proteins precipitated onto beads by the addition of ethanol to a final concentration of 80%. Samples were then shaken for 5 minutes at 1000 rpm and beads washed twice with 80% ethanol using a magnetic rack. Beads were then resuspended in 100mM tetraethylammonium bromide, pH 8.5 containing 0.5 μg of Trypsin/Lys-C (Promega, protein:protease ratio 1:100) and samples incubated at 37°C for 18 hours at 1000 rpm. The digestion supernatant was collected using a magnetic rack, beads washed with an equal volume of isopropanol to ensure complete recovery of peptides and samples acidified by the addition of trifluoroacetic acid (TFA, 1% final concentration) before being cleaned up using SDB-RPS (Supelco / 3M) Stagetips.[82–84] SDB-RPS material packed into 200 μl tips were washed with 30% methanol, 1% TFA before being equilibrated with 90% isopropanol, 1% TFA and samples loaded onto SDB-RPS columns by centrifugation. Columns were washed with 90% isopropanol, 1% TFA, followed by 90% ethyl acetate, 1% TFA and then 1% TFA. Samples were then eluted twice with 5% ammonium hydroxide, 80% acetonitrile before being dried by vacuum centrifugation.

Data independent acquisition (DIA) analysis

Peptide samples were re-suspended in Buffer A (2% acetonitrile, 0.1% TFA) and separated using a two-column chromatography set up composed of a PepMap100 C18 (20 mm × 75 μm) trap and a PepMap C18 (500 mm × 75 μm) analytical column (Thermo Fisher Scientific) coupled to a Orbitrap Eclipse Tribrid Mass Spectrometer (Thermo Fisher Scientific). Samples were loaded onto the trap column for 5 minutes at 5 μl/min with Buffer A (0.1% formic acid, 2% DMSO) and then separated over 125-minutes using the analytical column at 300 nl/min by altering the Buffer B composition (0.1% formic acid, 77.9% acetonitrile, 2% DMSO) concentration from 2% to 28% over 106 minutes, then to 40% over 9 minutes, and to 80% over 3 minutes. The composition was held at 80% B for 2 minutes, dropped to 2% over 2 minutes and held at this concentration for 3 minutes. The Orbitrap Eclipse Mass Spectrometer was operated in a data-independent mode automatically switching between the acquisition of a single Orbitrap MS scan (350-951 m/z, maximal injection time of 50 ms, an Automatic Gain Control (AGC) of 250% and a resolution of 120k) and the collection of 16 m/z DIA windows between 350 and 951 m/z (200−2,000 m/z, NCE 28%, maximal injection time of 54 ms, a AGC set to 2000% and a resolution of 30k). The proteomic data was searched with Spectronaut (Biognosys, version 17.1.221229) using the DIA library free analysis workflow allowing oxidation of Methionine and N-terminal acetylation as variable modifications as well as Carbamidomethyl as a fixed modification of cysteine with Trypsin as the digestion specificity. The protein label-free quantitation (LFQ) method was set to MaxLFQ with single hit proteins excluded, and the precursor PEP cut-off altered to 0.05 from the default 0.2 to improve quantitative accuracy. Searches were performed against the Mouse proteome (Uniprot Accession: UP000000589) supplemented with the Influenza A virus strain AX-31 H3N2_I000X Proteome (UniProtKB ID: 132504). Protein outputs from Spectronaut were processed using Perseus (version 1.6.0.7)[85] with missing values imputed based on the total observed protein intensities with a range of 0.3 σ and a downshift of 1.8 σ. Statistical analysis was undertaken within Perseus by grouping biological replicates together which were assessed using student t-tests with multiple hypothesis correction undertaken using a permutation-based FDR approach allowing an FDR of 5%.

Human plasma preparation and lipidomics

Day 1 plasma from SARS-CoV-2 PCR positive outpatient (n = 38) and hospitalized (n = 35) participants in the CIViC-19 cohort were carefully thawed on ice. Lipid extraction from 25 μL plasma was achieved by using a modified version of the Bligh and Dyer extraction

protocol.[86] Aliquots of stable internal standard mixtures-SPLASH Lipidomix Mass Spec Standard were spiked into all samples. Lipid extract (4 μL) was separated using a Thermo Accucore C30 column on a Thermo Vanquish Ultimate 3000 UPLC coupled to a Thermo Orbitrap Exploris 240 mass spectrometer (Thermo Fisher Scientific). Mass spectrometric (MS) data were operated in negative ionization electrospray modes. Data were acquired in full-scan mode (m/z 70 to 1,000) at a resolution of 120,000 for all samples. MS/MS data was collected in a sequence of separate runs operated by the intelligence-driven software AcquireX (Thermo Scientific, Waltham, MA) for FA(18:1) identification. The raw data were processed using LipidSearch (vers. 5.0; Thermo Scientific, Waltham, MA).

QUANTIFICATION AND STATISTICAL ANALYSIS

Where appropriate, data were tested for normality using a Shapiro-Wilk test. For nonparametric analysis between 2 groups, an unpaired two-tailed Mann-Whitney U test was used. For parametric analysis between 2 groups, an unpaired two-tailed Welch test was used. When 3 or more data sets were compared, a 2-way ANOVA with a Holms-Sidak post-hoc test was used. Analysis of survival data was performed using the Kaplan Meier method. A P value less than 0.05 was considered statistically significant. Specific details of statistical tests used in each experiment, including dispersion measures, are indicated within the figure legends and unless otherwise stated, were performed using Graph-Pad Prism, version 9.0.

Supplemental figures

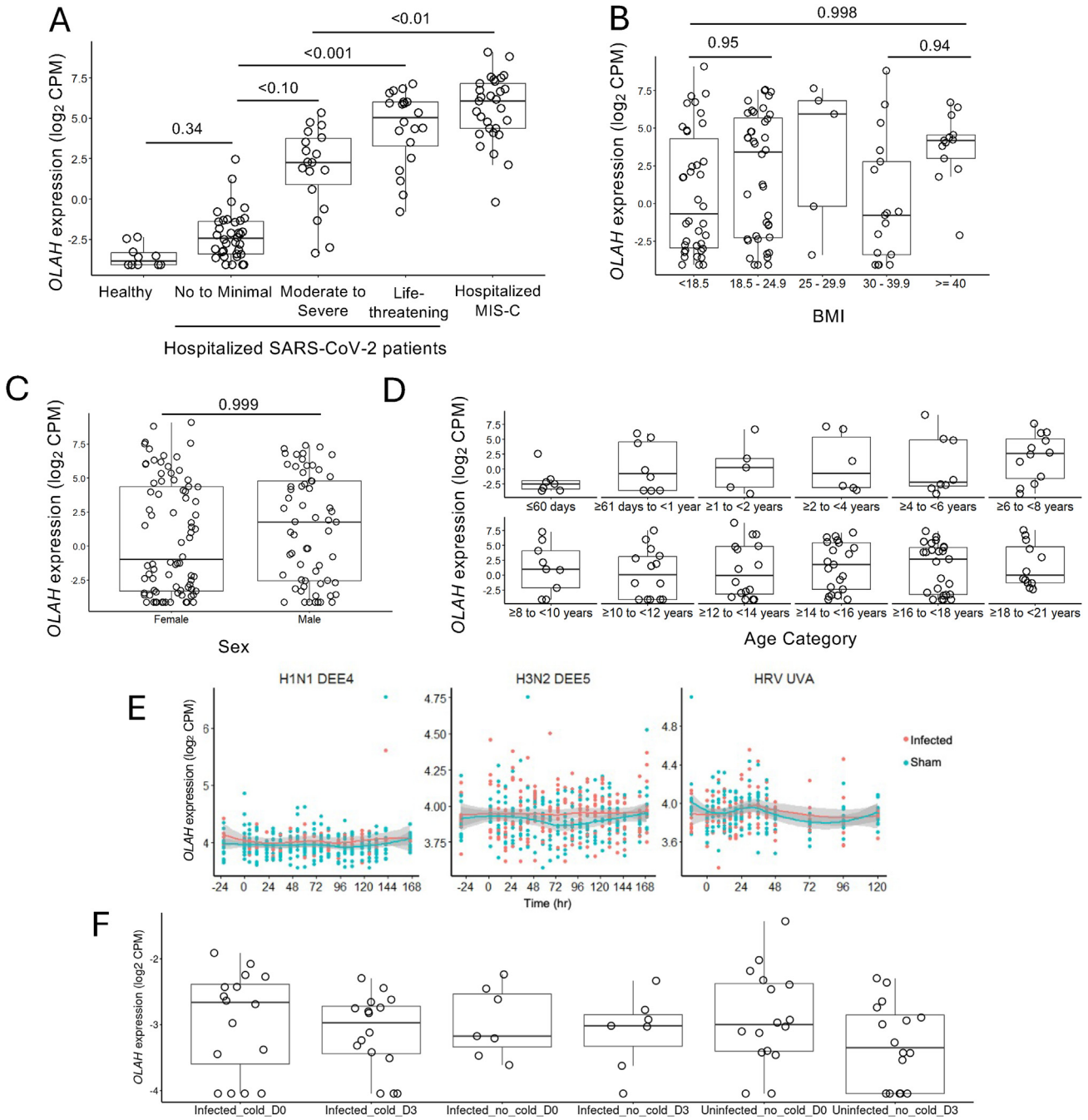

Figure S1. *OLAH* expression in SARS-CoV-2 patients stratified by BMI, age, and sex and across time for three human challenge models of mild respiratory infections, related to Figures 2A and 2F

(A) Analysis of *OLAH* expression from Figure 2A (right) was replicated to include BMI as a numeric covariate in the model (where patient BMI data was available; n = 113 of the original 143).

(B) Analysis of *OLAH* expression across commonly used BMI ranges (<18.5 = underweight; 18.5–24.9 = healthy weight; 25–29.9 = overweight; 30–30.9 = obese; ≥40 = severely obese). p values for three most visually distinct groups are shown. This analysis only includes 117 participants for whom BMI data were available.

(C) Analysis of *OLAH* expression stratified by gender (female = 82 samples, male = 61 samples).

(legend continued on next page)

(D) Analysis of *OLAH* expression across age categories (n = 143). Exact ages were not available in the provided metadata to protect patient identities.
(E) *OLAH* expression across three human challenge studies (H1N1 DEE4, n = 386; H3N2 DEE5, n = 461; HRV UVA n = 295) as LOESS curves with red corresponding to samples from infected participants and blue corresponding to samples from sham-infected participants. Linear mixed models were used to test for effects of time, infection status, and the interaction of time with infection status, with subject included as a random effect.
(F) Bulk RNA-seq from nasal curettage cells obtained from participants after controlled human RSV infection who became actively infected or did not exhibit active viral replication.

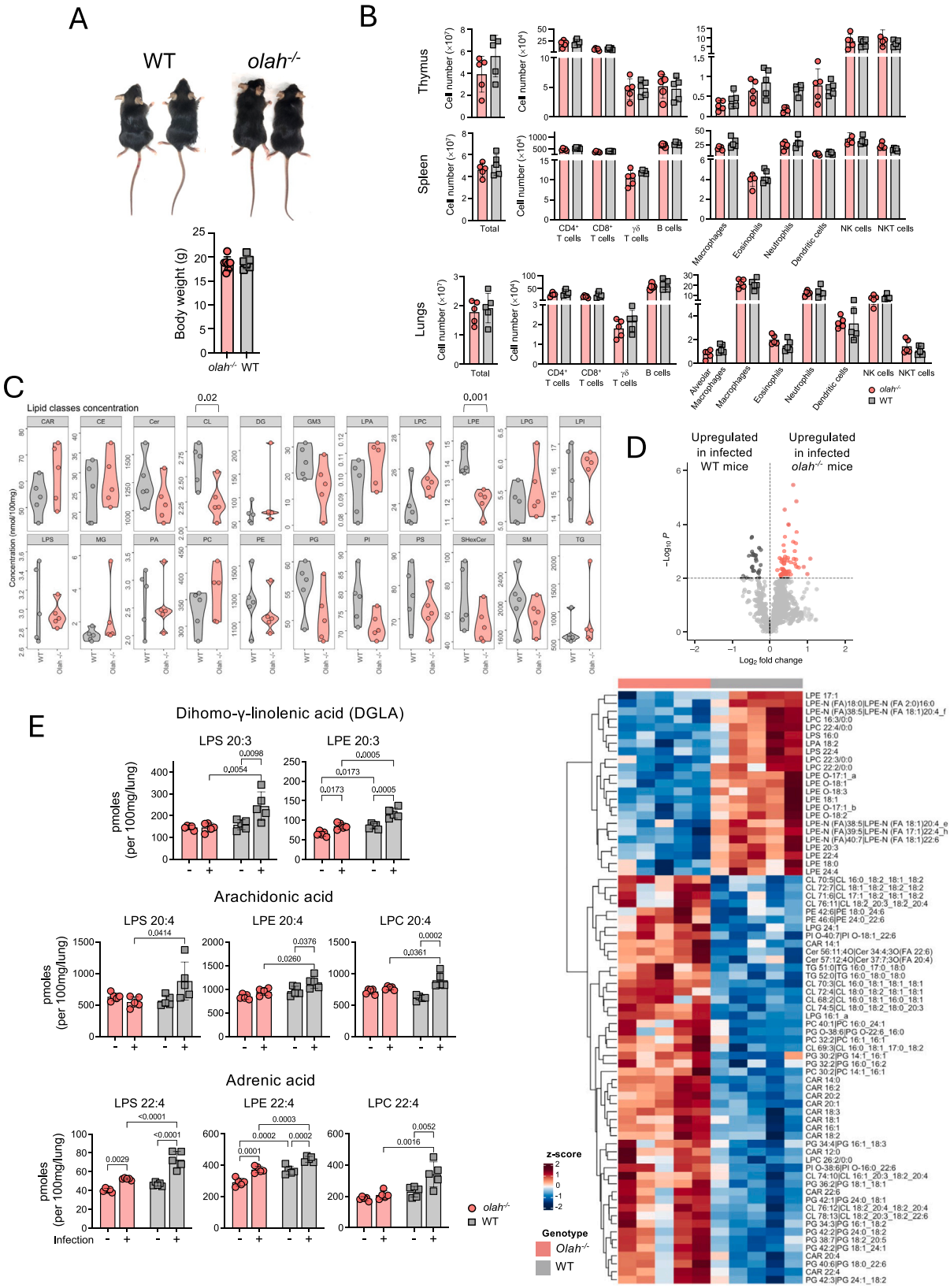

(legend on next page)

Figure S2. Phenotype and lung lipidomic profiles of WT and *olah*$^{-/-}$ mice, related to Figures 3C and 4

(A) Images of naive 7-week-old male WT and *olah*$^{-/-}$ mice and body weight profiles.

(B) Numbers of immune cell populations (mean ± SD) in organs of naive 7-week-old male WT and *olah*$^{-/-}$ mice.

(C) Levels of lipid classes in lungs from naive WT and *olah*$^{-/-}$ mice. Multiple t tests on $\log_{10}$ transformed data with FDR adjustment.

(D) Volcano plot of differentially expressed lipid species in lungs of infected WT and *olah*$^{-/-}$ mice at 1 day post-infection. Dark gray and red dots represent species that are upregulated (FDR < 0.01) in WT and *olah*$^{-/-}$ mice, respectively. The heatmap below depicts levels of differentially expressed lipid species (p <0.01).

(E) Levels of lipid species containing arachidonic acid (20:4), dihomo-γ-linolenic acid (20:3), and adrenic acid (22:4) in lungs of naive and infected WT and *olah*$^{-/-}$ mice. Two-way ANOVA with a Holms-Sidak post hoc test.

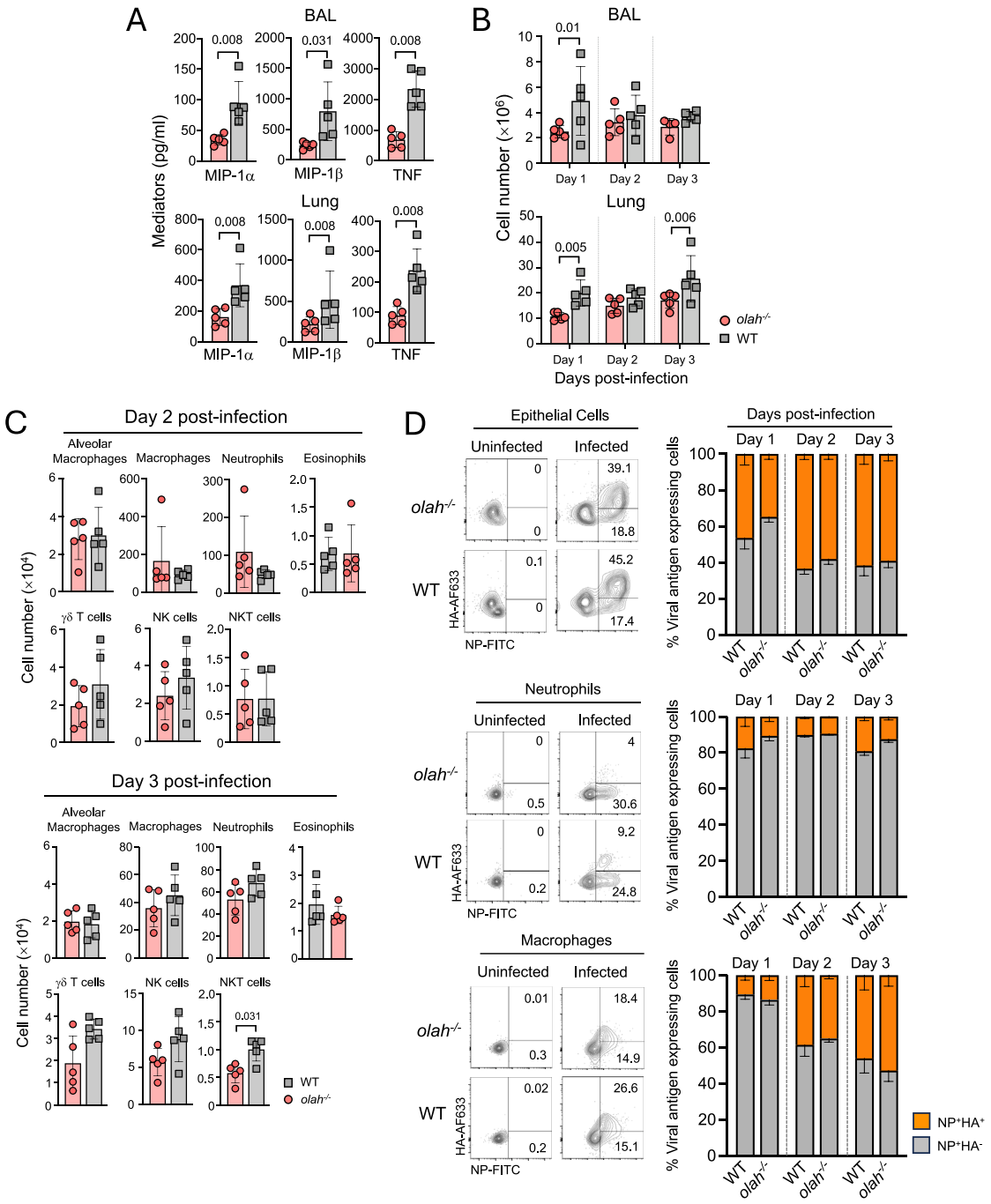

Figure S3. Innate immune responses in lungs of infected WT and *olah*$^{-/-}$ mice, related to Figures 4G and 4H

(A) Cytokine levels (mean ± SD) in BAL fluid and lungs of LD_{50}-infected mice (n = 5–6/group) at 1 day post-infection. Mann-Whitney test.

(B) Total cell numbers (mean ± SD) across 3 days of infection. Two-way ANOVA with a Holms-Sidak post hoc test.

(C) Numbers (mean ± SD) of innate immune cell populations on days 2 and 3 post-infection. Mann-Whitney test.

(D) Frequencies of lung epithelial cells, neutrophils, and macrophages (mean ± SEM) expressing viral antigens (intracellular NP and surface HA) in LD_{50}-infected mice (n = 8/group).

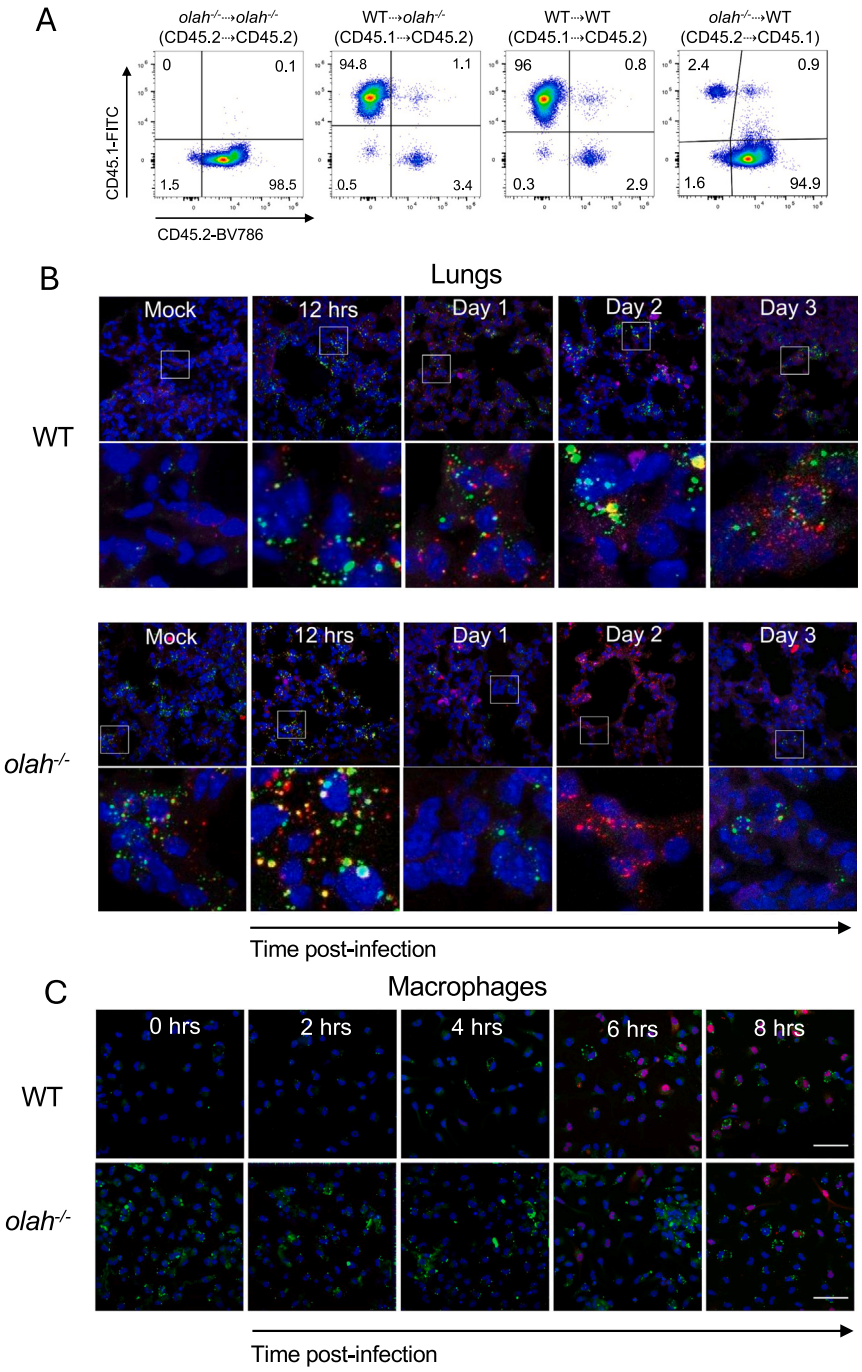

Figure S4. Reconstitution rates of bone marrow chimeras and representative microscopy images used to quantify lipid droplet numbers, related to Figures 5B–5F and 7A

(A) Expression of congenic markers (CD45.1 or CD45.2) on cells in blood of recipient mice following establishment of bone marrow chimeras. The congenic marker for each donor and recipient pairing is indicated in brackets.

(B) Representative merged images (incorporating DAPI nuclei staining) used to quantify lipid droplets in frozen lung sections of mice following LD50 infection. White framed boxes in each top image depict a field of view used for analysis of corresponding bottom images. Colours within each image represent DAPI (blue), BODIPY for lipid droplets (green), influenza NP (purple), and CD36 expression (red).

(C) Representative images used to quantify lipid droplets in macrophages following X31-infection. The white scale bar represents 50 μm.

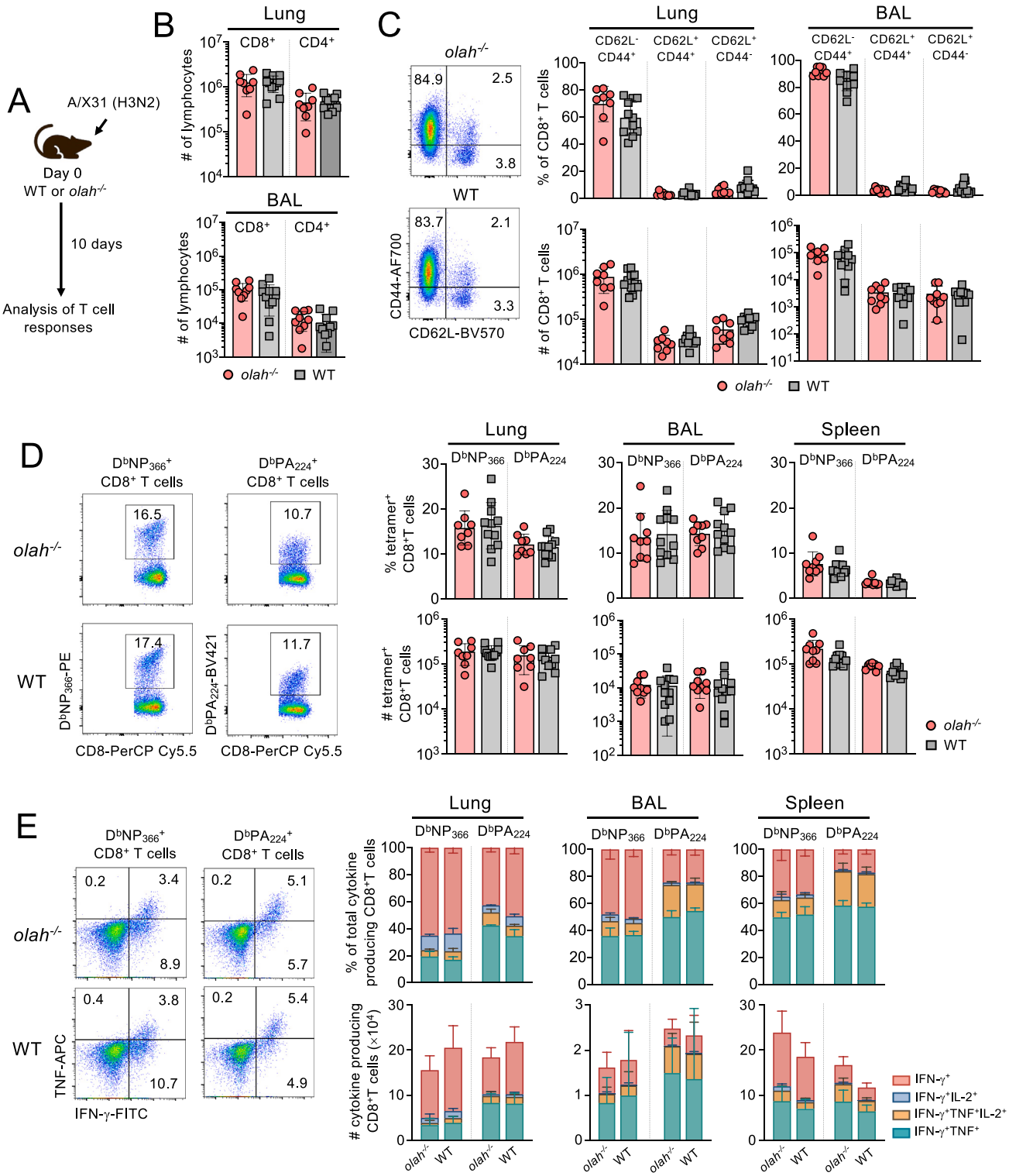

Figure S5. CD8$^+$ T cell responses in infected WT and *olah*$^{-/-}$ mice, related to Figures 4A–4D

(A) Organs were harvested from LD_{50}-infected mice (n = 8/group) 10 days post-infection and T cell responses analyzed.

(B) Total numbers of CD8$^+$ and CD4$^+$ T cells in lung and BAL (mean ± SD).

(C) Frequency and numbers (mean ± SD) of naive (CD62L$^+$CD44$^-$), effector (CD62L$^-$CD44$^+$), and memory (CD62L$^+$CD44$^+$) CD8$^+$ T cell populations.

(D) Frequency and numbers (mean ± SD) of tetramer$^+$ CD8$^+$ T cell populations in the lungs, BAL, and spleen.

(E) Frequency and numbers (mean ± SD) of NP_{366} and PA_{224}-peptide stimulated CD8$^+$ T cells secreting one or more cytokines the lungs, BAL, and spleen.

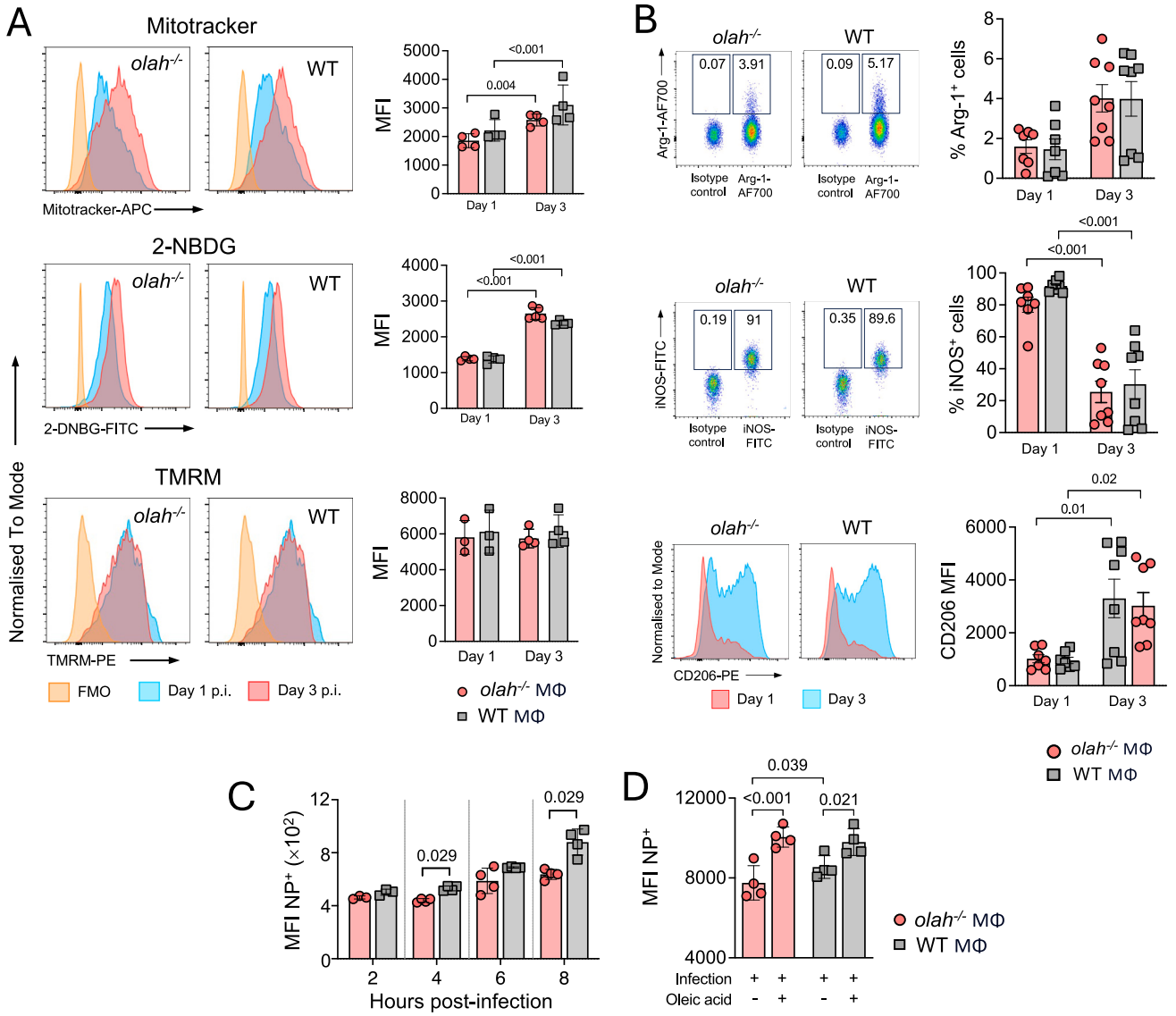

Figure S6. Expression of metabolic and polarization markers and NP expression in macrophages, related to Figure 6

(A) Expression of metabolic markers in lung macrophages in LD50-infected mice (n = 8/group) (mean ± SD) at 1 and 3 days post-infection (p.i.).

(B) Expression of polarization markers in lung macrophages in LD50-infected mice (n = 8/group) (mean ± SD) at 1 and 3 days p.i.

(C) Intracellular NP expression as mean fluorescent intensity (MFI) (mean ± SD) in peritoneal-derived macrophages over 8 h p.i. (n = 4/group/time point).

(D) Effects of oleic acid treatment on intracellular NP expression (mean ± SD) in peritoneal-derived macrophages 24 p.i.

Statistical analysis for (A)–(D) was performed by two-way ANOVA with Holms-Sidak post hoc test.

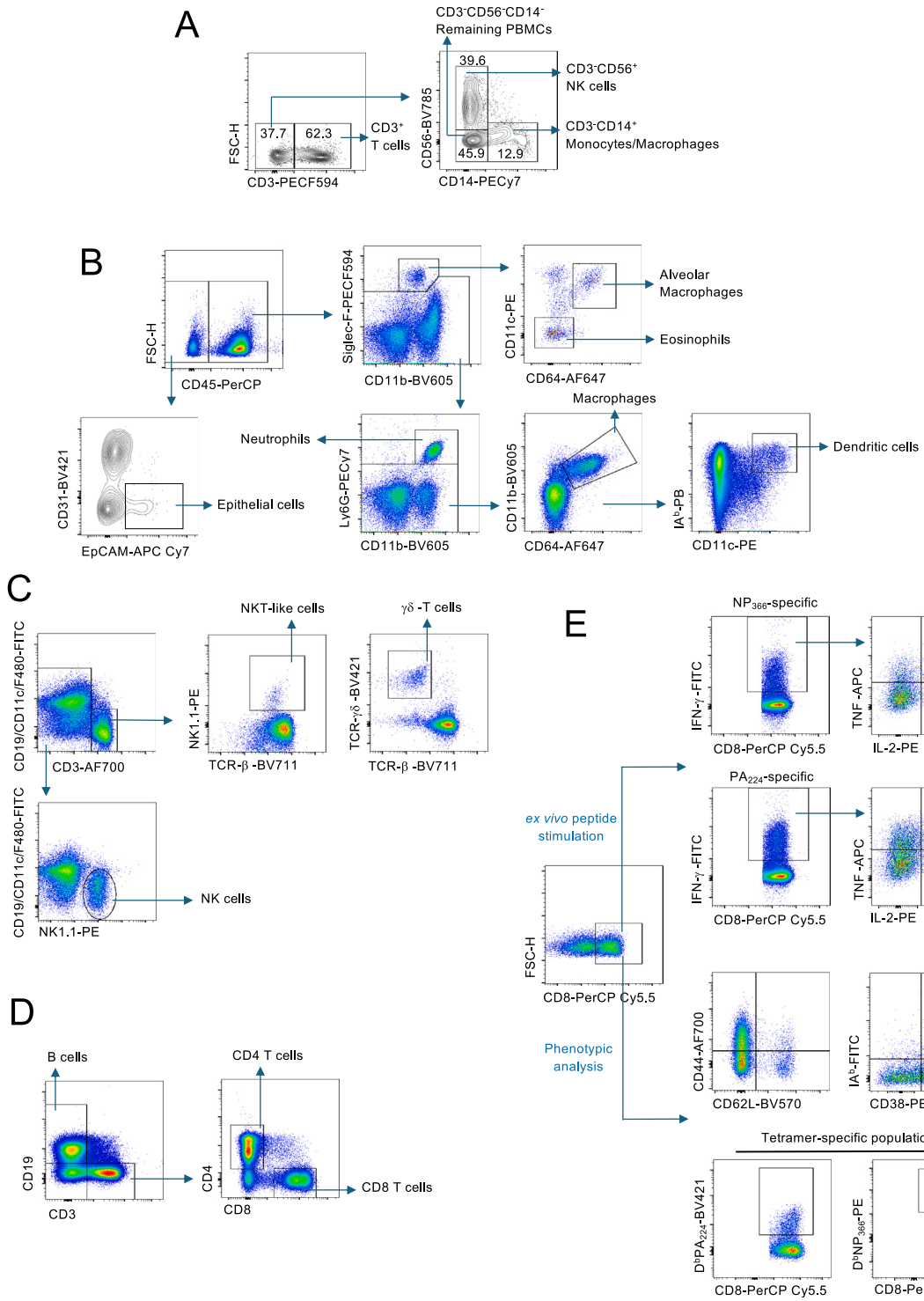

Figure S7. Gating strategy used to define cell populations, related to Figures 1H, 4H, 5A, and S5

(A) Gating strategy to define PBMC populations for Figure 1H.

(B and C) Gating strategy to define innate immune cell populations and respiratory epithelial cells for Figures 4H and 5A.

(D) Gating strategy to define adaptive immune populations for Figure S5.

(E) Gating strategy to define tetramer-specific, cytokine-producing $CD8^+$ T cells and subsets for Figure S5.